



# Resonant inelastic x-ray scattering of the $J_{\text{eff}} = \frac{1}{2}$ Mott insulator $\text{Sr}_2\text{IrO}_4$ from density functional theory

V. N. Antonov <sup>1,2,\*</sup>, D. A. Kukusta <sup>1</sup> and L. V. Bekenov <sup>1</sup>

<sup>1</sup>*G. V. Kurdyumov Institute for Metal Physics of the N.A.S. of Ukraine, 36 Academician Vernadsky Boulevard, UA-03142 Kyiv, Ukraine*

<sup>2</sup>*Max-Planck-Institute for Solid State Research, Heisenbergstrasse 1, 70569 Stuttgart, Germany*



(Received 13 October 2023; revised 13 February 2024; accepted 29 March 2024; published 10 April 2024)

We have investigated the electronic structure of  $\text{Sr}_2\text{IrO}_4$  within density functional theory using the generalized gradient approximation while considering strong Coulomb correlations in the framework of the fully relativistic spin-polarized Dirac linear muffin-tin orbital band-structure method. We have investigated x-ray absorption spectra, x-ray magnetic circular dichroism, and resonant inelastic x-ray scattering (RIXS) spectra at the Ir  $K$ ,  $L_3$ ,  $M_3$ ,  $M_5$ , and O  $K$  edges. The calculated results are in good agreement with experimental data. The RIXS spectrum of  $\text{Sr}_2\text{IrO}_4$  at the Ir  $L_3$  edge possesses a sharp feature  $<1.5$  eV corresponding to transitions within the Ir  $t_{2g}$  levels. The excitation located from 2 to 5 eV is due to  $t_{2g} \rightarrow e_g$  transitions. The third wide structure situated at 5–12 eV appears due to charge transfer transitions. We have found that the theory reproduces well the shape and energy position of the low-energy feature in the oxygen O  $K$  RIXS spectrum, but to obtain the correct positions of the second and third peaks, a self-interaction-correction-like orbital-dependent potential  $V_l$  must be included in the Hamiltonian to correct the position of the oxygen  $2p$  band. We have found that the dependence of the RIXS spectrum at the oxygen  $K$  edge on the incident photon energy and the momentum transfer vector  $\mathbf{Q}$  is much stronger than the correspondent dependence at the Ir  $L_3$  edge.

DOI: [10.1103/PhysRevB.109.165120](https://doi.org/10.1103/PhysRevB.109.165120)

## I. INTRODUCTION

In  $5d$  transition metal compounds, the energy scale of the spin-orbit coupling (SOC) is comparable with the on-site Coulomb interaction and the crystal-field energy. Due to the strong competition between these interactions, fascinating electronic states can arise. SOC in such systems splits the  $t_{2g}$  orbitals into a quartet ( $J_{\text{eff}} = \frac{3}{2}$ ) and a doublet ( $J_{\text{eff}} = \frac{1}{2}$ ) [1–3]. In  $5d^5$  ( $\text{Ir}^{4+}$ ) iridium oxides, the quartet  $J_{\text{eff}} = \frac{3}{2}$  is fully occupied, and the relatively narrow  $J_{\text{eff}} = \frac{1}{2}$  doublet occupied by one electron can be split by moderate Hubbard  $U_{\text{eff}}$  with opening a small band gap called the relativistic Mott gap [4–6]. Iridates have been at the center of an intensive search in recent years for phenomena such as topological insulators [7–10], Mott insulators [1,4,5,11,12], Weyl semimetals [13–15], and quantum spin liquids [1,16].

Among iridium compounds,  $\text{Sr}_2\text{IrO}_4$ , a single-layer member of the Ruddlesden-Popper series iridates, is of special interest. It has a quasi-two-dimensional (2D) square-lattice perovskite structure and is a spin-orbit  $J_{\text{eff}} = \frac{1}{2}$  Mott insulator [4]. Additionally, it has structural and physical similarities with  $\text{La}_2\text{CuO}_4$ , a parent compound to high- $T_c$  cuprates, such as the presence of a pseudogap [4,17,18], similar Fermi

surfaces and Fermi arcs (in electron- and hole-doped compounds) [19,20],  $d$ -wave symmetry [21,22], electron-boson coupling [23], and similarities in the magnetic ordering and magnetic excitations [24,25]. However, the superconductivity in  $\text{Sr}_2\text{IrO}_4$  has not been found yet [26].

There are some energy band calculations for  $\text{Sr}_2\text{IrO}_4$  [4,5,27–41]. Pröpper *et al.* [42] presented the energy band structure and optical spectra calculated in the  $U$ -corrected local spin density approximation (LSDA+ $U$ ) approach in the frame of the fully relativistic linear muffin-tin orbital (LMTO) method. They found that the best agreement between the calculated and experimental optical absorption spectra was obtained for Hubbard  $U_{\text{eff}} = 1.3$  eV. The authors analyzed the experimental spectra in terms of  $J_{\text{eff}} = \frac{1}{2}$  and  $\frac{3}{2}$  interband transitions. Martins *et al.* [5], Arita *et al.* [29], Liu *et al.* [33], and Zhang *et al.* [31] presented the energy band structure calculations for  $\text{Sr}_2\text{IrO}_4$  using dynamical mean field theory (DMFT) as well as the  $U$ -corrected generalized gradient approximation (GGA+ $U$ ) method. Within DMFT, the insulating gap was found to be equal to 0.4 eV [31], in good agreement with the calculations of Pröpper *et al.* [42]. The GGA+ $U$  band structures are in fairly good agreement with the DMFT spectral functions; however, there are some differences. In the DMFT calculation, the topmost valence state at the  $X$  point is  $\sim 40$  meV closer to  $E_F$  than the first valence state at the  $\Gamma$  point, in agreement with recent angle-resolved photoemission spectroscopy (ARPES) measurements [30] but in contrast with the GGA+ $U$  results [31]. This is because the filled orbitals (here,  $J_{\text{eff}} = \frac{3}{2}$ ) tend to be repelled from the Fermi level in DMFT. The dispersion of the energy bands is more pronounced in the GGA+ $U$  calculations in comparison with the DMFT spectral functions, especially for empty  $t_{2g}$

\*victor.antonov13@gmail.com

Published by the American Physical Society under the terms of the [Creative Commons Attribution 4.0 International license](https://creativecommons.org/licenses/by/4.0/). Further distribution of this work must maintain attribution to the author(s) and the published article's title, journal citation, and DOI. Open access publication funded by Max Planck Society.

states. The band gaps slightly differ from each other in some symmetry points. On the other hand, the DMFT approach produces a similar optical conductivity spectrum to the LSDA+ $U$  optical spectrum in Ref. [42].

In this paper, we focus our attention on the resonant inelastic x-ray scattering (RIXS) properties in  $\text{Sr}_2\text{IrO}_4$ . Since the publication by Kao *et al.* on NiO [43], the RIXS method has shown remarkable progress in condensed matter physics research as a spectroscopic technique to record the momentum and energy dependence of inelastically scattered photons in complex materials [44]. RIXS nowadays has rapidly come to the forefront of experimental photon science. It provides a direct probe of spin and orbital states and dynamics. RIXS has a number of unique features in comparison with other spectroscopic techniques. It covers a large scattering phase space and requires only small sample volumes. It also is bulk sensitive, polarization dependent, as well as element and orbital specific [44].

Depending on the x-ray resonant energy, RIXS can be divided into two classes: soft and hard x rays [44]. For high-atomic-number transition metal elements, such as  $5d$  transition metal compounds, the  $K$ - and  $L$ -edge resonant energies are in the hard x-ray region. For such spectra, high-quality single crystals are needed as the key optical elements. The RIXS resolution crucially depends on the availability of a high-quality single crystal with a Bragg diffraction peak close to backscattering at the energy of the  $L$  edge of the targeted element. This requirement severely limits the application of RIXS, and thus, by far the majority of hard x-ray RIXS studies have been focused on  $5d$  iridates [45–50] and osmates [51–53]. In a soft RIXS setup, the x-ray energy range is usually below  $\sim 2$  keV [54]. The  $L$  edges of the  $3d$  transition metal elements all fall below this energy scale. The energy resolution in the soft x-ray region is relatively high. For example, the combined energy resolution was 150 meV at the Ni  $L_3$  edge ( $\sim 850$  eV) in  $\text{Ta}_2\text{NiSe}_5$  [55]. The best energy resolution currently achieved for RIXS at the oxygen  $K$  edge ( $\sim 530$  eV) of the common ligand atoms is  $\sim 45$ – $50$  meV [56,57], which is much better than the majority of  $5d$  elements probed using  $L$ -edge RIXS in the hard x-ray region to date. We should mention, however, that in recent years, experimentalists have achieved remarkable progress in increasing the resolution for hard RIXS spectra. For example, Kim *et al.* [58] have obtained the total resolution of 34.2 meV at the Ir  $L_3$  edge in  $\text{Sr}_2\text{IrO}_4$ . Such a resolution permits direct measurements of single-magnon excitations as well as other many-body excitations in strongly correlated systems.

In the x-ray absorption spectroscopy (XAS), x-ray magnetic circular dichroism (XMCD), and RIXS processes at the O  $K$  edge, the  $1s$ -core level is involved. The exchange splitting of the  $1s$ -core state is extremely small, and SOC is absent in the O  $1s$  orbitals; therefore, only the exchange and spin-orbit splitting of the  $2p$  states is responsible for the observed spectra at the oxygen  $K$  edge. On the other hand, the oxygen valence  $2p$  states of the surrounding ligand atoms are sensitive to the electronic states at neighboring sites because of their delocalized nature. They strongly hybridize with the  $5d$  orbitals. Due to such hybridization combined with high SOC at the  $5d$  ion, information on the elementary excitations can be extracted using an indirect RIXS process at the O  $K$  edge [57]. Although

O  $K$  RIXS has a much smaller penetration depth ( $\sim 100$  nm) than  $5d$   $L$  RIXS, comparison between O  $K$  and Ir  $L_3$  spectra measured on  $\text{Sr}_2\text{IrO}_4$  suggests that they have comparable counting efficiency [57]. The lower penetration depth of soft x-rays has its own advantages, providing high sensitivity to ultrathin samples such as films. Soft x-ray RIXS at the O  $K$  edge is a promising method for studying the electronic and magnetic excitations in  $5d$  compounds. There are several experimental investigations of the RIXS spectra at the oxygen  $K$  edge [54,57–59] in  $\text{Sr}_2\text{IrO}_4$ . The Ir  $L_3$  RIXS spectra in this oxide are investigated in Refs. [24,58–63].

We carry out here a detailed study of the electronic structure, XAS, XMCD, and RIXS spectra of  $\text{Sr}_2\text{IrO}_4$  in terms of the density functional theory (DFT). Our study sheds light on the important role of band structure effects and transition metal  $5d$  – oxygen  $2p$  hybridization in the spectral properties in  $5d$  oxides. The energy band structure and the spectra of  $\text{Sr}_2\text{IrO}_4$  are investigated in the *ab initio* approach using the fully relativistic spin-polarized Dirac LMTO band-structure method. We use both the generalized gradient approximation (GGA) and the GGA+ $U$  approach to assess the sensitivity of the RIXS results to different treatment of the correlated electrons.

This paper is organized as follows. The crystal structure of  $\text{Sr}_2\text{IrO}_4$  and computational details are presented in Sec. II. Section III presents the electronic and magnetic structures of  $\text{Sr}_2\text{IrO}_4$ . In Sec. IV, the theoretical investigations of the XAS, XMCD, and RIXS spectra of  $\text{Sr}_2\text{IrO}_4$  at the Ir  $K$ ,  $L_3$ ,  $M_3$ , and  $M_5$  edges are presented; the theoretical results are compared with experimental measurements. In Sec. V, we present the theoretical investigations of the XAS and RIXS spectra at the O  $K$  edge. Finally, the results are summarized in Sec. VI.

## II. COMPUTATIONAL DETAILS

### A. XMCD

Magneto-optical (MO) effects refer to various changes in the polarization state of light upon interaction with materials possessing a net magnetic moment, including rotation of the plane of linearly polarized light (Faraday, Kerr rotation), and the complementary differential absorption of left and right circularly polarized light (circular dichroism). In the near-visible spectral range, these effects result from excitation of electrons in the conduction band. Near x-ray absorption edges, or resonances, MO effects can be enhanced by transitions from well-defined atomic core levels to transition symmetry-selected valence states.

Within the one-particle approximation, the absorption coefficient  $\mu_j^\lambda(\omega)$  for incident x-ray polarization  $\lambda$  and photon energy  $\hbar\omega$  can be determined as the probability of electronic transitions from initial core states with the total angular momentum  $j$  to final unoccupied Bloch states:

$$\mu_j^\lambda(\omega) = \sum_{m_j} \sum_{nk} |(\Psi_{nk} | \Pi_\lambda | \Psi_{jm_j})|^2 \times \delta(E_{nk} - E_{jm_j} - \hbar\omega) \theta(E_{nk} - E_F), \quad (1)$$

where  $\Psi_{jm_j}$  and  $E_{jm_j}$  are the wave function and the energy of a core state with the projection of the total angular momentum

$m_j$ ;  $\Psi_{n\mathbf{k}}$  and  $E_{n\mathbf{k}}$  are the wave function and the energy of a valence state in the  $n$ th band with the wave vector  $\mathbf{k}$ ; and  $E_F$  is the Fermi energy.

Here,  $\Pi_\lambda$  is the electron-photon interaction operator in the dipole approximation:

$$\Pi_\lambda = -e\boldsymbol{\alpha}\mathbf{a}_\lambda, \quad (2)$$

where  $\boldsymbol{\alpha}$  are the Dirac matrices, and  $\mathbf{a}_\lambda$  is the  $\lambda$  polarization unit vector of the photon vector potential, with  $a_\pm = 1/\sqrt{2}(1, \pm i, 0)$ ,  $a_\parallel = (0, 0, 1)$ . Here,  $+$  and  $-$  denote, respectively, left and right circular photon polarizations with respect to the magnetization direction in the solid. Then x-ray magnetic circular and linear dichroisms are given by  $\mu_+ - \mu_-$  and  $\mu_\parallel - (\mu_+ + \mu_-)/2$ , respectively. More detailed expressions of the matrix elements in the electric dipole approximation may be found in Refs. [64–66]. The matrix elements due to magnetic dipole and electric quadrupole corrections are presented in Ref. [66].

### B. RIXS

In the direct RIXS process [44], the incoming photon with energy  $\hbar\omega_{\mathbf{k}}$ , momentum  $\hbar\mathbf{k}$ , and polarization  $\boldsymbol{\epsilon}$  excites the solid from the ground state  $|g\rangle$  with energy  $E_g$  to the intermediate state  $|I\rangle$  with energy  $E_I$ . During relaxation, an outgoing photon with energy  $\hbar\omega_{\mathbf{k}'}$ , momentum  $\hbar\mathbf{k}'$ , and polarization  $\boldsymbol{\epsilon}'$  is emitted, and the solid is in state  $|f\rangle$  with energy  $E_f$ . As a result, an excitation with energy  $\hbar\omega = \hbar\omega_{\mathbf{k}} - \hbar\omega_{\mathbf{k}'}$  and momentum  $\hbar\mathbf{q} = \hbar\mathbf{k} - \hbar\mathbf{k}'$  is created. Our implementation of the code for the calculation of the RIXS intensity uses Dirac four-component basis functions [67] in the perturbative approach [68]. RIXS is the second-order process, and its intensity is given by

$$I(\omega, \mathbf{k}, \mathbf{k}', \boldsymbol{\epsilon}, \boldsymbol{\epsilon}') \propto \sum_f \left| \sum_I \frac{\langle f | \hat{H}'_{\mathbf{k}'\boldsymbol{\epsilon}'} | I \rangle \langle I | \hat{H}'_{\mathbf{k}\boldsymbol{\epsilon}} | g \rangle}{E_g - E_I} \right|^2 \times \delta(E_f - E_g - \hbar\omega), \quad (3)$$

where the RIXS perturbation operator in the dipole approximation is given by the lattice sum  $\hat{H}'_{\mathbf{k}\boldsymbol{\epsilon}} = \sum_{\mathbf{R}} \hat{\boldsymbol{\alpha}}\boldsymbol{\epsilon} \exp(-i\mathbf{k}\mathbf{R})$ , where  $\boldsymbol{\alpha}$  are the Dirac matrices. The sum over the intermediate states  $|I\rangle$  includes the contributions from different spin-split core states at the given absorption edge. The matrix elements of the RIXS process in the frame of the fully relativistic Dirac LMTO method were presented in Ref. [69].

### C. Crystal structure

The powder neutron diffraction measurements show that  $\text{Sr}_2\text{IrO}_4$  possesses the tetragonal  $I4_1/acd$  perovskite structure (group number 142) [Fig. 1(a)] [70]. The  $\text{IrO}_6$  octahedra in  $\text{Sr}_2\text{IrO}_4$  are rigidly aligned, just as the  $\text{CuO}_6$  octahedra in cuprates, rotated by  $\sim 11^\circ$  about the  $c$  axis in the  $a$ - $b$  plane [Fig. 1(b)], and have a local distortion of 4.5% axial elongation.

Atomic positions of  $\text{Sr}_2\text{IrO}_4$  at 10 K (the lattice constants  $a = 5.48164 \text{ \AA}$ ,  $c = 25.80019 \text{ \AA}$ ) for Sr, Ir,  $\text{O}_1$ , and  $\text{O}_2$  are  $(0, \frac{1}{4}, z_{\text{Sr}})$ ,  $(0, \frac{1}{4}, \frac{3}{8})$ ,  $(0, \frac{1}{4}, z_{\text{O}})$ , and  $(x, x + \frac{1}{4}, z_{\text{O}})$ , respectively, with  $x = 0.1996$ ,  $z_{\text{Sr}} = 0.5506$ , and  $z_{\text{O}} = 0.4548$  [70]. The oxygen atoms surrounding the Ir sites provide an octahedral

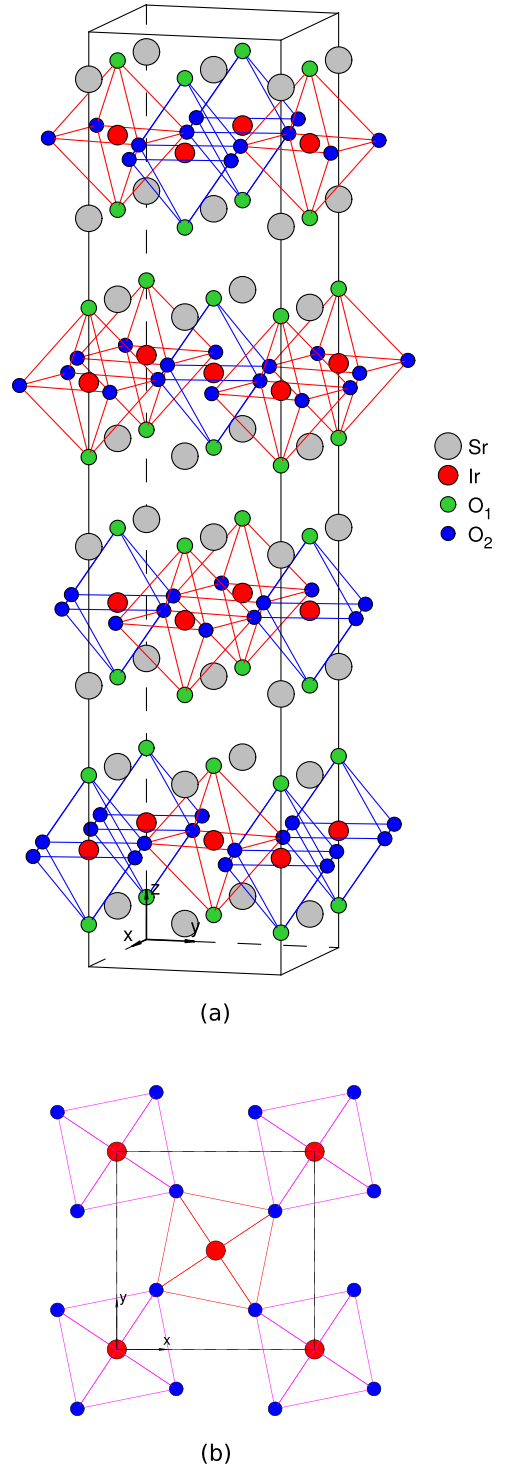


FIG. 1. (a) The schematic representation of the body-centered tetragonal  $I4_1/acd$  (group number 142)  $\text{Sr}_2\text{IrO}_4$  crystal structure [70]; (b) the positions of ions in the  $\text{IrO}_2$  plane perpendicular to the  $c$  axis.

environment. The Ir- $\text{O}_1$  and Ir- $\text{O}_2$  interatomic distances are equal to 2.05886 and 1.97704  $\text{\AA}$ , respectively. Around each Ir atom, there are eight Sr atoms with the Ir-Sr distance  $d_{\text{Ir-Sr}} = 3.34615 \text{ \AA}$ . The Ir-Ir distance  $d_{\text{Ir-Ir}} = 3.87610 \text{ \AA}$ .

Note that, in our electronic structure calculations, we rely on experimentally measured internal parameters  $x$ ,  $z_{\text{Sr}}$ , and  $z_{\text{O}}$  and lattice constants because they are well established for this material and are probably still more accurate than those obtained from DFT can be.

#### D. Calculation details

The details of the computational method are described in our previous papers [69,71–73], and here, we only mention several aspects. The band structure calculations were performed using the fully relativistic LMTO method [65,74]. This implementation of the LMTO method uses four-component basis functions constructed by solving the Dirac equation inside an atomic sphere [67]. The exchange-correlation functional of the GGA type was used in the version of Perdew, Burke, and Ernzerhof [75]. The Brillouin zone integration was performed using the improved tetrahedron method [76]. The basis consisted of Ir and Sr  $s$ ,  $p$ ,  $d$ , and  $f$  and O  $s$ ,  $p$ , and  $d$  LMTOs.

To consider the electron-electron correlation effects, we used in this paper the relativistic generalization of the rotationally invariant version of the LSDA+ $U$  method [77] which considers that, in the presence of spin-orbit coupling, the occupation matrix of localized electrons becomes nondiagonal in spin indexes. Hubbard  $U$  was considered an external parameter and varied from 0.65 to 3.65 eV. We used in our calculations the value of exchange Hund coupling  $J_H = 0.65$  eV obtained from constrained LSDA calculations [78,79]. Thus, the parameter  $U_{\text{eff}} = U - J_H$ , which roughly determines the splitting between the lower and upper Hubbard bands, varied between 0 and 3.0 eV. We adjusted the value of  $U$  to achieve the best agreement with the experiment.

In the RIXS process, an electron is promoted from a core level to an intermediate state, leaving a core hole. As a result, the electronic structure of this state differs from that of the ground state. To reproduce the experimental spectrum, the self-consistent calculations should be carried out including a core hole. Usually, the core-hole effect has no impact on the shape of XAS at the  $L_{2,3}$  edges of  $5d$  systems and just a minor effect on the XMCD spectra at these edges [65]. However, the core hole has a strong effect on the RIXS spectra in transition metal compounds [69,80]; therefore, we consider it.

### III. ELECTRONIC AND MAGNETIC STRUCTURES

We performed GGA, GGA+SO, and GGA+SO+ $U$  calculations of the electronic and magnetic structures of  $\text{Sr}_2\text{IrO}_4$  for the experimental crystal structure [70]. Our GGA+SO band structure calculations show that the canted noncollinear (NC) antiferromagnetic (AFM) configuration with the spins in the  $ab$  plane (see Fig. 2) possesses the lowest total energy in comparison with the nonmagnetic, ferromagnetic (FM), or AFM configuration along the  $c$  direction (Table I). The NC angles equal to  $\theta_{\text{Ir}_1} = 90^\circ$ ,  $\phi_{\text{Ir}_1} = 13.8^\circ$  and  $\theta_{\text{Ir}_2} = 90^\circ$ ,  $\phi_{\text{Ir}_2} = 166.2^\circ$  are in good agreement with experimental values of  $12.8^\circ \pm 0.8^\circ$  [81] and  $13^\circ \pm 1^\circ$  [82] (for the  $\text{Ir}_1$  site) and with previous DFT results [4,83]. This NC-AFM $_{ab}$  configuration produces a weak net magnetic moment  $M$  of  $\sim 0.09 \mu_B/\text{Ir}$  (experimental  $M = 0.06\text{--}0.1 \mu_B/\text{Ir}$  [11,84]).

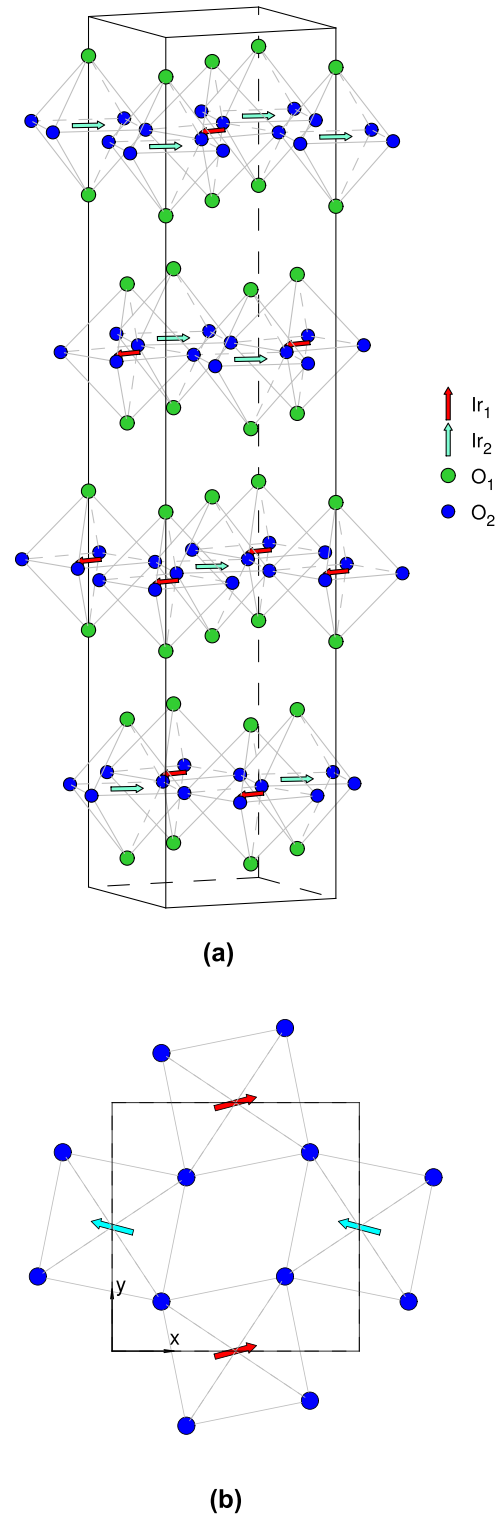


FIG. 2. (a) The canted noncollinear AFM $_{ab}$  ordering in  $\text{Sr}_2\text{IrO}_4$  calculated in the GGA+SO+ $U$  calculations; (b) the orientation of the Ir magnetic moments in the  $\text{IrO}_2$  plane perpendicular to the  $c$  axis.

Figure 3 establishes a picture of the SOC-driven Mott transition in  $\text{Sr}_2\text{IrO}_4$ . In the absence of SOC, the partially filled bands of predominantly  $t_{2g}$  orbital character would lead to a metallic ground state [Figs. 3(a)–3(d)].

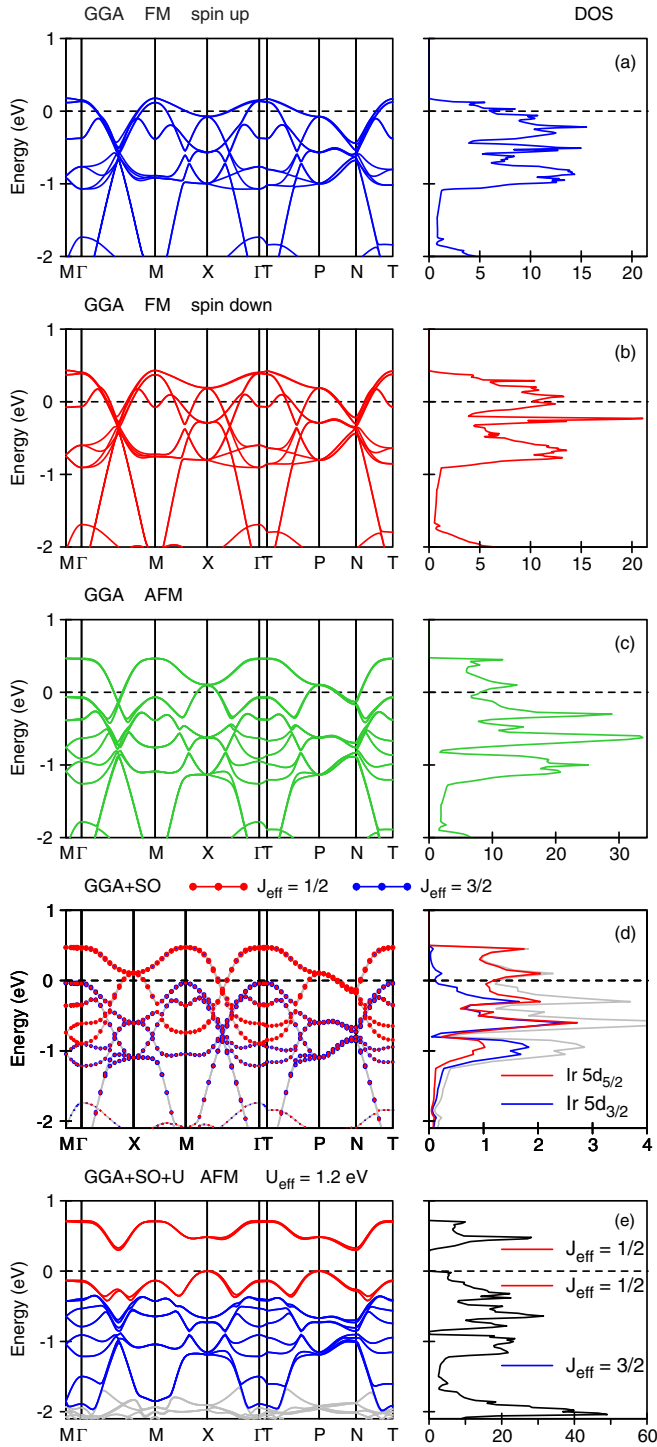


FIG. 3. The  $t_{2g}$  energy band structure of  $\text{Sr}_2\text{IrO}_4$  calculated in the generalized gradient approximation (GGA) approach without spin-orbit coupling (SOC) for the ferromagnetic (FM) ordering for the (a) spin-up and (b) spin-down states. (c) Energy bands for the antiferromagnetic (AFM) ordering in the GGA approach. (d) Fully relativistic Dirac GGA+SO approach. The bands crossing the Fermi level which have almost pure  $d_{5/2}$  character (open red circles) are formed by  $t_{2g}$  states with  $J_{\text{eff}} = \frac{1}{2}$ . (e)  $t_{2g}$  energy bands calculated in the GGA+SO+ $U$  approach with  $U_{\text{eff}} = 1.2$  eV for the canted noncollinear  $\text{AFM}_{ab}$  ordering.

TABLE I. The total energy  $E_{\text{total}}$  per formula unit (in eV) calculated in the GGA for the nonmagnetic configuration ( $\text{NM}_{\text{GGA}}$ ) and the GGA+SO for  $\text{NM}_{\text{GGA}+\text{SO}}$ ,  $\text{FM}_{001}$ ,  $\text{AFM}_{001}$ , and the canted NC AFM ordering in the  $ab$  plane ( $\text{NC-AFM}_{ab}$ ) defined relative to the  $\text{NC-AFM}_{ab}$  configuration.

$\text{NM}_{\text{GGA}}$	$\text{NM}_{\text{GGA}+\text{SO}}$	$\text{FM}_{001}$	$\text{AFM}_{001}$	$\text{NC-AFM}_{ab}$
1.184	0.459	0.135	0.003	0.0

The fully relativistic GGA+SO bands are presented in Fig. 3(d) by circles proportional in size to their orbital character projected onto the basis set of Ir  $d_{3/2}$  (the relativistic quantum number  $\kappa = 2$ , the blue curve) and  $d_{5/2}$  ( $\kappa = -3$ , the red curve) states. In the strong SOC limit, the  $t_{2g}$  band splits into effective total angular momentum  $J_{\text{eff}} = \frac{1}{2}$  doublet and  $J_{\text{eff}} = \frac{3}{2}$  quartet bands. As a result, with the filled  $J_{\text{eff}} = \frac{3}{2}$  band and one remaining electron in the  $J_{\text{eff}} = \frac{1}{2}$  band, the system is effectively reduced to a half-filled  $J_{\text{eff}} = \frac{1}{2}$  single-band system. The functions of the  $J_{\text{eff}} = \frac{3}{2}$  quartet are dominated by  $d_{3/2}$  states with some weight of  $d_{5/2}$  ones. The  $J_{\text{eff}} = \frac{1}{2}$  functions are almost completely given by the linear combinations of  $d_{5/2}$  states [Fig. 3(d)]. The  $J_{\text{eff}} = \frac{1}{2}$  spin-orbit integrated states form a narrow band so that even small Hubbard  $U$  opens up a Mott gap, making  $\text{Sr}_2\text{IrO}_4$  a  $J_{\text{eff}} = \frac{1}{2}$  Mott insulator [Fig. 3(e)].

The GGA+SOC+ $U$  solution captures the salient features of the insulating state of  $\text{Sr}_2\text{IrO}_4$ , reproducing the electronic band structure measured by ARPES [4] and the canted AFM structure measured by resonant x-ray scattering (RXS) [11]. From these calculations, the insulating gap clearly opens up only as a result of the combined effects of SOC and Hubbard  $U$ . However, there has been much debate over the correlation effects that drive the gap opening and whether  $\text{Sr}_2\text{IrO}_4$  can be classified as a genuine Mott insulator or a Slater insulator [29], where the gap opens up primarily because of magnetic order. Although there have been several experimental reports concerning this issue, these results are still controversial. The temperature dependence of the gap below  $T_N$  seems to be consistent with typical Slater-type behavior [27,29,85–87]. On the other hand, the temperature dependence of the resistivity shows no significant changes at Néel temperature  $T_N$  [88], strongly indicating that  $\text{Sr}_2\text{IrO}_4$  is a Mott-type insulator. Additionally, the scanning tunneling spectroscopy shows an unusually large intrinsic insulating gap of 620 meV [89,90]. Such a big gap implies that  $\text{Sr}_2\text{IrO}_4$  is unlikely a Slater insulator since the magnetic coupling energy is merely  $\sim 60$  meV [24,84], which is too small to account for the large gap. Additionally, while the long-range magnetic ordering temperature is  $T_N = 240$  K, resistivity measurements do not reveal a metallic state up to 600 K [88], suggesting that the magnetic ordering is unlikely the source of the insulating behavior. Moreover, the time-resolved photocarrier dynamics experiments suggest that Slater and Mott characteristics coexist in  $\text{Sr}_2\text{IrO}_4$  [91]. Many theoretical and experimental studies also conclude that  $\text{Sr}_2\text{IrO}_4$  has mixed Slater and Mott peculiarities [26,91,92]. The results of the theoretical study

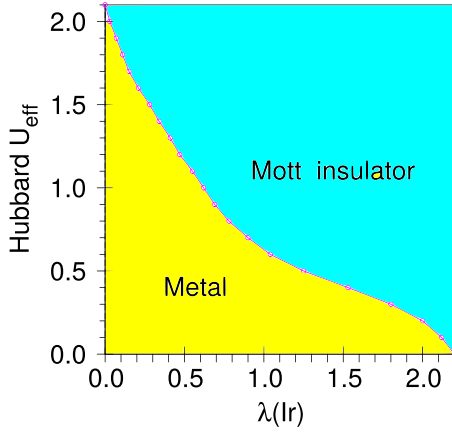


FIG. 4. The phase diagram in the  $U_{\text{eff}}$ -SOC plane for  $\text{Sr}_2\text{IrO}_4$ . The solid-circled line presents critical  $U_{\text{eff}}^c$  values calculated in the GGA+SO+ $U$  approach for the canted NC-AFM $_{ab}$  order for which the energy band opens up. This line separates metal and Mott insulator states connected via a first-order phase transition.

of the insulating mechanism in a multiorbital Hubbard model using a variational Monte Carlo method obtained by Watanabe *et al.* [93] indicate that  $\text{Sr}_2\text{IrO}_4$  is a moderately correlated AFM insulator located between Slater- and Mott-type insulators.

Our theoretical calculations show that, for the nonmagnetic solution, the energy gap does not open up for any, even very large, Hubbard parameter  $U$  in  $\text{Sr}_2\text{IrO}_4$ . For the FM ordering without SOC, the gap opens up at the critical value  $U_{\text{eff}}^c = 4.0$  eV. The phase transition from the FM to AFM ordering leads to a significant reduction of the density of states (DOS) at  $E_F$ , which is situated close to the local minimum [see Fig. 3(c)]. Therefore, for the collinear AFM ordering without SOC, the gap opens up at smaller  $U_{\text{eff}}^c = 2.2$  eV. With SOC, the gap opens up at  $U_{\text{eff}}^c = 1.7$  eV and 0.64 eV for the collinear FM and AFM ordering, respectively. For the ground state NC canted NC-AFM $_{ab}$  ordering, the gap opens up for even smaller  $U_{\text{eff}}^c = 0.58$  eV. We can conclude that the magnetic ordering plays an important role in the gap formation in  $\text{Sr}_2\text{IrO}_4$ ; therefore, this oxide has mixed Slater and Mott character.

Figure 4 presents a phase diagram in the  $U_{\text{eff}}$ -SOC plane for  $\text{Sr}_2\text{IrO}_4$ . To obtain this diagram, we tune the SOC term for the Ir  $5d$  orbitals. A scaling factor  $\lambda$  in the SOC term of the Hamiltonian is introduced in the second variational step [94]. In this way, we can enhance the effect of SOC by taking  $\lambda > 1$  or reduce it by taking  $\lambda < 1$ . For  $\lambda = 0$ , there is no SOC at all, while  $\lambda = 1$  refers to the self-consistent reference value. The solid-circled line in Fig. 4 separates metal and Mott insulator states, which are connected via a first-order phase transition, calculated in the GGA+SO+ $U$  approach for the canted NC-AFM $_{ab}$  order. The energy gap opens up for  $U_{\text{eff}}^c = 2.1$  eV for  $\lambda = 0$  and for  $\lambda = 2.2$  with  $U_{\text{eff}}^c = 0$  eV. The greater the value of  $U_{\text{eff}}$ , the lower the value of  $\lambda$  is for the phase transition.

Figure 5 presents the experimentally measured real part of the optical conductivity (open magenta circles),  $\sigma_{1xx}$ , [95] for the energy  $< 2$  eV in  $\text{Sr}_2\text{IrO}_4$  compared with the theoretical spectra calculated in the GGA+SO+ $U$  approach for different

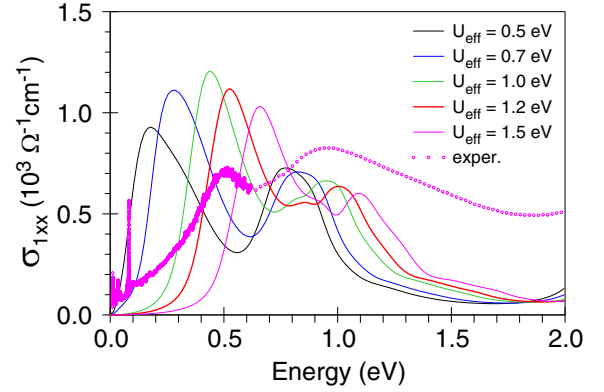


FIG. 5. The experimentally measured real part of the optical conductivity (open magenta circles),  $\sigma_{1xx}$ , [95] (in  $10^3 \Omega^{-1} \text{cm}^{-1}$ ) in  $\text{Sr}_2\text{IrO}_4$  of the in-plane response compared with the theoretical spectra calculated in the GGA+SO+ $U$  approach for different  $U_{\text{eff}}$  values.

$U_{\text{eff}}$  values. The experimental optical absorption consists of two peaks at  $\sim 0.5$  and 1.0 eV. We found that the low-energy peak is derived from transitions between initial and final bands formed by pure  $J_{\text{eff}} = \frac{1}{2}$  states near band boundaries, e.g., around the X point or the  $P$ - $N$  high-symmetry line. The AFM ordering of Ir moments within the  $ab$  plane stabilized by the on-site Coulomb repulsion  $U$  causes a gap opening near the zone boundary between two pairs of bands which show nearly parallel dispersion which ensures high joint DOS for the interband transitions responsible for the low-energy peak. This is in line with previous theoretical calculations [31,42] and experimental photoemission results [30]. The high-energy peak located  $\sim 1$  eV is dominated by a contribution from transitions with  $J_{\text{eff}} = \frac{3}{2}$  initial states. Our calculations give the lower absorption peak about twice as strong as the higher-energy one, while in the experimental spectra the strength is approximately the same for both. A similar trend was also observed by Pröpper *et al.* [42] and Kim *et al.* [96]. The latter authors relate this to an interband mixing of  $J_{\text{eff}} = \frac{3}{2}$  and  $J_{\text{eff}} = \frac{1}{2}$  states, which reflects the itinerancy of the system, i.e., the hybridization of Ir  $5d$  states via neighboring oxygen  $2p$  states. It is interesting to note that the DMFT+ $U$  approach used by Zhang *et al.* [31] improves the relative intensities between the low- and high-energy peaks of  $\sigma_{1xx}$ . We found that the best agreement between the calculated and experimentally measured energy positions of the optical absorption peaks can be achieved for  $U_{\text{eff}} = 1.2$  eV (Fig. 5). This value is slightly smaller in comparison with the result of Pröpper *et al.* [42] of 1.3 eV due to different exchange-correlation potentials used: the GGA type in the version of Perdew, Burke, and Ernzerhof [75] in our work and the Perdew-Wang LDA type [97] in Ref. [42].

Figure 6 presents the partial DOS in  $\text{Sr}_2\text{IrO}_4$  calculated in the GGA+SO+ $U$  approach with  $U_{\text{eff}} = 1.2$  eV. Five electrons occupy the  $t_{2g}$ -type low-energy band (LEB) manifold in the energy interval from  $-1.5$  eV to  $E_F$  in  $\text{Sr}_2\text{IrO}_4$ . The empty  $t_{2g}$  states [the upper-energy band (UEB)] consist of one peak and occupy the energy range from 0.41 to 0.82 eV (see Fig. 6). The  $e_g$ -type states of Ir are distributed far above the Fermi

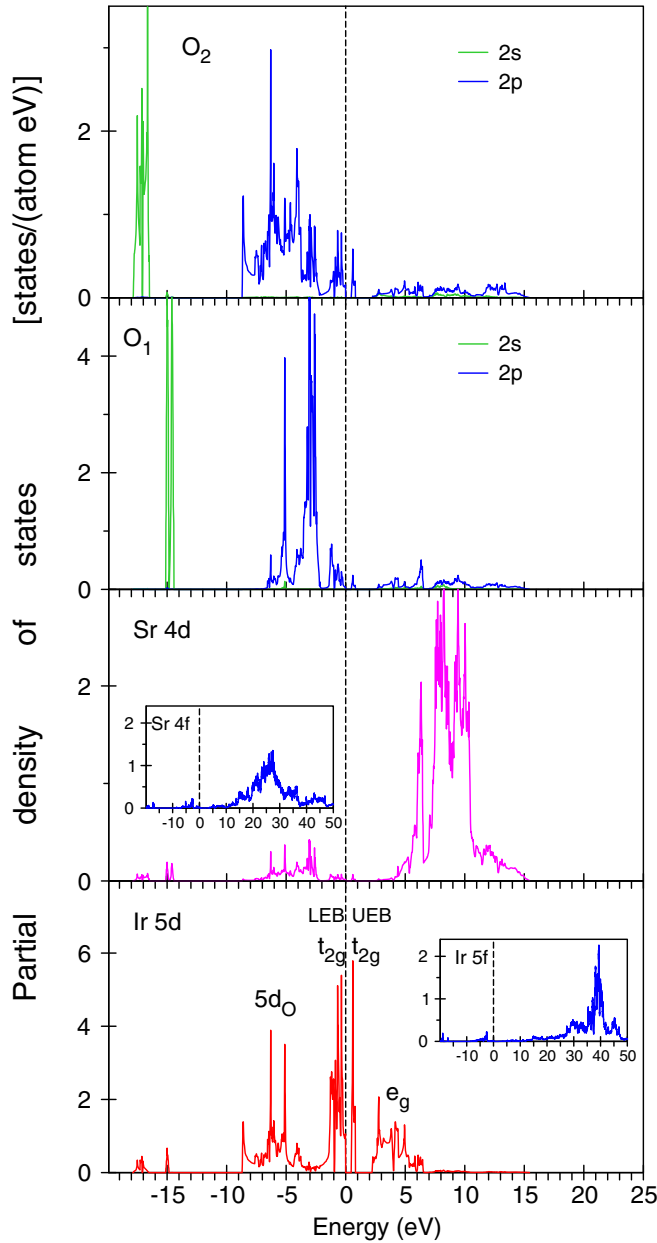


FIG. 6. The partial density of states (DOS) for  $\text{Sr}_2\text{IrO}_4$  calculated in the GGA+SO+ $U$  ( $U_{\text{eff}} = 1.2$  eV) approach.

level from 2.2 to 5.1 eV. The 4d states of Sr ions are mostly situated above the Fermi level from 5.3 to 10.8 eV.

The electronic structures of apical  $\text{O}_1$  and in-plane  $\text{O}_2$  ions significantly differ from each other. The apical  $\text{O}_1$  2s states consist of two very narrow peaks situated at  $-15.1$  and  $-14.4$  eV. The in-plane  $\text{O}_2$  2s states possess a relatively wider two peak structure from  $-17.9$  to  $-16.5$  eV. The  $\text{O}_1$  2p states are situated just below Ir LEB between  $-3.5$  and  $-2.1$  eV. There is also a narrow peak at  $-5.2$  eV. The in-plane  $\text{O}_2$  2p states occupy a relatively wide energy interval from  $-8.7$  to  $-3.6$  eV. The small peaks in the close vicinity of the Fermi level from  $-1.5$  eV to  $E_F$  and from 0.41 to 0.82 eV are due to the strong hybridization between O 2p and Ir  $t_{2g}$  LEB and UEB, respectively.

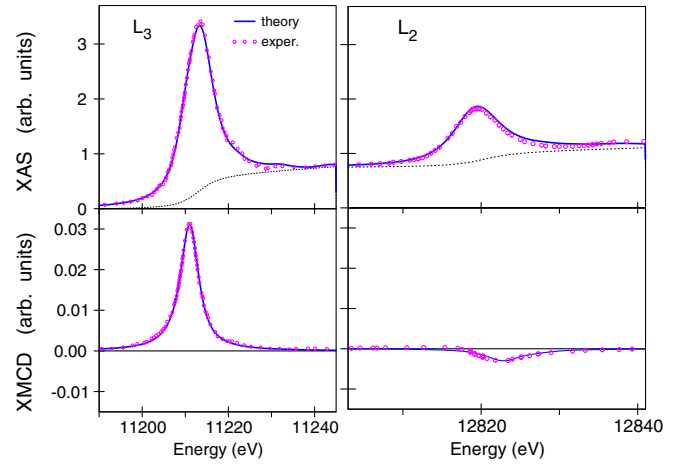


FIG. 7. The experimental x-ray absorption (upper panels) and x-ray magnetic circular dichroism (XMCD) spectra (lower panels) at the Ir  $L_{2,3}$  edges in the  $\text{Sr}_2\text{IrO}_4$  thin film (magenta circles) [98] measured at 6 K under a 0.8 T magnetic field compared with the theoretically calculated spectra in the GGA+SO+ $U$  approach (full blue curves). The dotted black curves in the upper panels show the background scattering intensity.

The occupation number of 5d electrons in the Ir atomic sphere in  $\text{Sr}_2\text{IrO}_4$  is equal to 6.3, which is much larger than the expected value of five  $t_{2g}$  electrons. The excessive charge is provided by the tails of oxygen 2p states. These  $5d_O$  states are located at the bottom of oxygen 2p states from  $-8.7$  to  $-3.1$  eV and play an essential role in the RIXS spectrum at the Ir  $L_3$  edge (see Sec. IV).

The theoretically calculated spin  $M_s$ , orbital  $M_l$ , and total  $M_{\text{total}}$  magnetic moments using the GGA+SO+ $U$  approach ( $U_{\text{eff}} = 1.2$  eV) for the AFM solution are equal to  $0.2647 \mu_B$ ,  $0.4447 \mu_B$ , and  $0.7094 \mu_B$ , respectively. The spin and orbital magnetic moments at the Sr site are relatively small ( $M_s = 0.0007 \mu_B$  and  $M_l = 0.0015 \mu_B$ ). The magnetic moments for apical  $\text{O}_1$  ions are equal to  $M_s = 0.0294 \mu_B$ ,  $M_l = 0.0254 \mu_B$ . For in-plane  $\text{O}_2$  ions the magnetic moments almost vanish.

## IV. Ir XMCD AND RIXS SPECTRA

### A. $L_3$ and $M_3$ edges

Figure 7 presents the experimentally measured XAS (the upper panel) and XMCD spectra (the lower panel) at the Ir  $L_{2,3}$  edges for  $\text{Sr}_2\text{IrO}_4$  [98] (open circles) compared with the theoretically calculated ones in the GGA+SO+ $U$  ( $U_{\text{eff}} = 1.2$  eV) approach (full blue curves). The theoretically calculated Ir  $L_{2,3}$  XAS and XMCD spectra are in good agreement with the experiment. The isotropic XAS spectra are dominated by the empty  $e_g$  states with a smaller contribution from the empty  $t_{2g}$  orbitals at lower energy. The XMCD spectra, however, mainly come from the  $t_{2g}$  orbitals ( $J_{\text{eff}} = \frac{1}{2}$ ). This results in a shift between the maxima of the XAS and XMCD spectra.

Due to the importance of SOC effects in iridates, it is natural to quantify the strength of the SO interactions in these compounds. One method of accomplishing this is provided by the XAS. Van der Laan and Thole showed that the so-called branching ratio (BR) =  $I_{L_3}/I_{L_2}$  ( $I_{L_{2,3}}$  is the integrated

intensity of the isotropic XAS at the  $L_{2,3}$  edges) is an important quantity in the study of  $5d$  oxides related to the SO interaction [99]. The BR is directly related to the ground-state expectation value of the angular part of the spin-orbit coupling  $\langle \mathbf{L} \cdot \mathbf{S} \rangle$  through  $BR = (2+r)/(1-r)$ , with  $r = \langle \mathbf{L} \cdot \mathbf{S} \rangle / n_h$  and  $n_h$  is the number of holes in  $5d$  states [99]. As a result, XAS provides a direct probe of SO interactions, which is complementary to other techniques such as the magnetic susceptibility, electron paramagnetic resonance, and Mossbauer spectroscopy (which probe SOC through the value of the Lande  $g$  factor). In the limit of negligible SOC effects the statistical branching ratio  $BR = 2$ , and the  $L_3$  white line is twice the size of the  $L_2$  feature [99]. The measured BR in  $\text{Sr}_2\text{IrO}_4$  is  $\sim 4.1$  [98], which differs significantly from the statistical  $BR = 2$  in the absence of orbital magnetization in  $5d$  states. A strong deviation from 2 indicates a strong coupling between the local orbital and spin moments. Our DFT calculations produce  $BR = 3.56$  for the GGA+SO+ $U$  ( $U_{\text{eff}} = 1.2$  eV) approach, which is rather close to the experimental data of Haskell *et al.* [98].

The RIXS spectra at Ir  $L_{2,3}$  occur from a local excitation between the filled and empty  $5d$  states. More precisely, the incoming photon excites a  $2p_{1/2}$  core electron ( $L_2$  spectrum) or  $2p_{3/2}$  one ( $L_3$  spectrum) into an empty  $5d$  state which is followed by the de-excitation from the occupied  $5d$  state into the core level. Because of the dipole selection rules, apart from  $6s_{1/2}$  states (which have a small contribution to RIXS due to relatively small  $2p \rightarrow 6s$  matrix elements [65]), only  $5d_{3/2}$  states occur for  $L_2$  RIXS, whereas for  $L_3$  RIXS,  $5d_{5/2}$  states also contribute. Although the  $2p_{3/2} \rightarrow 5d_{3/2}$  radial matrix elements are only slightly smaller than the  $2p_{3/2} \rightarrow 5d_{5/2}$  ones, the angular matrix elements strongly suppress the  $2p_{3/2} \rightarrow 5d_{3/2}$  contribution [65]. Therefore, the RIXS spectrum at the Ir  $L_3$  edge can be viewed as interband transitions between  $5d_{5/2}$  states.

Figure 8 shows the theoretical RIXS spectrum of  $\text{Sr}_2\text{IrO}_4$  at the Ir  $L_3$  edge for  $t_{2g} \rightarrow t_{2g}$  transitions in comparison with different experimental data. The energy resolution of RIXS used in the earlier study of Ishii *et al.* [60] (exper. 1) was insufficient to resolve the dispersion and the intrinsic linewidth of the low-energy modes associated with the intra- $t_{2g}$  excitations. The measurements of J. Kim *et al.* [24] (exper. 2) and Clancy *et al.* [63] (exper. 3) are very similar, and additionally, an elastic peak centered at zero energy possesses two peaks  $\alpha$  and  $\beta$  at 0.2 and 0.6 eV, respectively. Our calculations are in good agreement with these measurements. We found that the low-energy peak  $\alpha$  is due to interband transitions between occupied and empty Ir  $J_{\text{eff}} = \frac{1}{2}$  states (the dashed red curve). These transitions also contribute to the second high-energy peak  $\beta$  together with  $J_{3/2} \rightarrow J_{1/2}$  transitions (the dashed green curve).

Kim *et al.* [100] detected three peaks A, B, and C at 0.1, 0.5, and 0.6 eV, respectively (experiments 5, 6, and 7 in Fig. 8). These three RIXS spectra were measured at three different incident angles  $\phi$  of  $8^\circ$ ,  $45^\circ$ , and  $82^\circ$ . They correspond to three-dimensional  $\mathbf{Q}$  of  $(-3.5, 3, 25.5)$ ,  $(0.5, 0, 34)$ , and  $(3.5, 3, 25.5)$ , respectively, in reciprocal lattice units. The peak B shows strong dependency of its intensity on  $\phi$  through the change in the incident and outgoing x-ray polarizations relative to the sample surface and thereby the RIXS

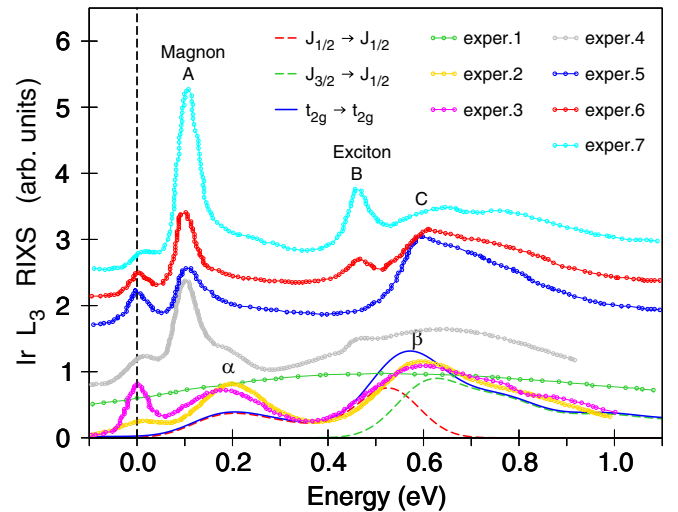


FIG. 8. The theoretical resonant inelastic x-ray scattering (RIXS) spectrum of  $\text{Sr}_2\text{IrO}_4$  at the Ir  $L_3$  edge for  $t_{2g} \rightarrow t_{2g}$  transitions (the full red curve) and transitions between  $J_{\text{eff}}$  states (dashed blue and green curves) calculated in the GGA+SO+ $U$  approach ( $U_{\text{eff}} = 1.2$  eV) in comparison with different experimental data: exper. 1 [60], exper. 2 [24], exper. 3 [63], exper. 4 [58], exper. 5 [100], exper. 6 [100], and exper. 7 [100].

matrix elements. This peak B is strongly enhanced (completely suppressed) by tuning  $\phi$  to the normal (grazing) incidence geometry. The energy position of the peak C in the Kim *et al.* [100] measurements coincides with the peak  $\beta$  from the measurements in Refs. [24,63] (experiments 2 and 3). These peaks have the same physical origin. It is interesting to note that recent measurements with very high resolution of Kim *et al.* [58] (exper. 4 in Fig. 8) show all the peaks A, B, and  $\beta$  ( $\equiv C$ ). Due to the strong dependence of the RIXS spectrum at the Ir  $L_3$  edge on the momentum transfer vector  $\mathbf{Q}$  and polarization, the peaks A and B can be detected only for specific experimental geometry.

The peak A at  $\sim 0.1$  eV was attributed in Ref. [100] to magnon excitations. We can note that Nichols *et al.* [89] also detected a single-magnon excitation at the energy of 0.105 eV using scanning tunneling microscope measurements. The peak B was attributed to an excitonic excitation in Refs. [58,100]. The NC-AFM<sub>ab</sub> ordering stabilized by the on-site Coulomb repulsion  $U$  causes a gap opening near the zone boundary between two pairs of bands which show nearly parallel dispersion [see Fig. 3(e)], which can indicate possible creation of an exciton in  $\text{Sr}_2\text{IrO}_4$ . The theoretical description of magnon and exciton spectra demands a many-body approach beyond the one-particle approximation, such as the Bethe-Salpiter equation for exciton spectra and calculations of the magnon dispersion and the electron-magnon interaction for magnon spectra.

There have been several attempts in the literature to calculate the exciton and magnetic excitations in  $\text{Sr}_2\text{IrO}_4$ . Most of such theoretical investigations have been carried out within localized spin models [24,101–104]. The magnon dispersion in  $\text{Sr}_2\text{IrO}_4$  has been theoretically studied in terms of the  $J_{\text{eff}} = \frac{1}{2}$  quantum Heisenberg AFM on a square lattice by Kim *et al.* [24]. Igarashi and Nagao [105] introduced a multiorbital



tight-binding model and calculated the one-electron energy band within the Hartree-Fock approximation and the Green's functions for particle-hole pair excitations within the random phase approximation. The RIXS spectra were evaluated from the Green's functions within the fast collision approximation. Analyzing the low-energy region, the authors found a two-peak structure which may be interpreted as the split modes of a magnon. They also obtained several  $\delta$ -function peaks, which arise from the bound states around the bottom of the energy continuum. They may be called exciton modes. Although these characteristics are in qualitative agreement with the experiment, the full description of the  $L_3$ -edge RIXS spectrum was not obtained. In another approach, the exciton dispersion was obtained in analogy with the hole motion in an AFM background [24,96]; however, the bare exciton dispersion was neglected in this approach. Mohapatra *et al.* [36] and Mohapatra and Singh [106,107] investigated correlated motion of interorbital particle-hole excitations across the renormalized SO gap, along with detailed comparison with RIXS data for the spin-orbit exciton modes in  $\text{Sr}_2\text{IrO}_4$ .

We should mention that RIXS spectra can also be very sensitive to sample quality. For example, the insulating energy gap  $\Delta$  in  $\text{Sr}_2\text{IrO}_4$  (after subtraction of magnon and other possible many-body excitations) can vary strongly for different samples. The gaps as low as  $\sim 0.1$  eV have been reported [70,108]. On the other hand, ARPES measurements do not agree with this value since the maximum of the valence band is already lower than  $-0.1$  eV [4,30]. Optical conductivity and RIXS studies both yield  $\Delta \leq 0.4$  eV [4,24,27]. Dai *et al.* [90] have presented scanning tunneling microscopy and spectroscopy experiments on  $\text{Sr}_2\text{IrO}_4$ . Their local DOS (LDOS) measurements show a rather large intrinsic gap of 0.62 eV.

An approach from first principles for a unified description of both magnon and exciton excitations on the same footing with considering RIXS matrix elements is highly desirable.

Figure 9 (the lower panel) shows the experimental RIXS spectrum (open green circles) measured by Ishii *et al.* [60] at the Ir  $L_3$  edge in  $\text{Sr}_2\text{IrO}_4$  in a wide energy interval up to 7.5 eV compared with the theoretically calculated one in the GGA+SO+ $U$  approach ( $U_{\text{eff}} = 1.2$  eV). The intensive peak at  $\sim 3.4$  eV (the red curve in Fig. 9) is due to  $t_{2g} \rightarrow e_g$  transitions. The next fine structure from 4.5 to 12 eV (the magenta curve) is due to  $5d_O \rightarrow t_{2g}, e_g$  transitions.

Figure 9 (the upper panel) shows the theoretically calculated RIXS spectrum at the Ir  $M_3$  edge in  $\text{Sr}_2\text{IrO}_4$ . The  $M_3$  spectrum possesses very similar fine structures as the Ir  $L_3$  spectrum but with much smaller intensity due to corresponding matrix elements.

Figure 10 shows the Ir  $L_3$  RIXS spectrum as a function of incident photon energy  $E_i$  above the corresponding edge with the momentum transfer vector  $\mathbf{Q} = (0, 0, 33)$  in reciprocal lattice units. We found that the low-energy fine structure corresponding to intra- $t_{2g}$  excitations is slightly decreased when the incident photon energy changes from 11 210 to 11 212 eV, while the high-energy peak corresponding to the  $t_{2g} \rightarrow e_g$  transitions is monotonically increased (the upper panel of Fig. 10). A similar trend was observed in the measurements of Ishii *et al.* [60]. They measured the RIXS spectra of  $\text{Sr}_2\text{IrO}_4$  at two representative incident photon energies in the interval of

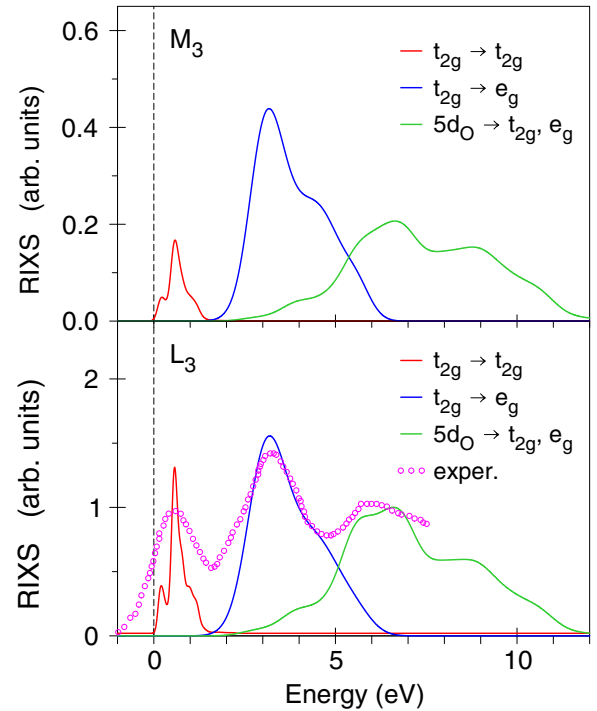


FIG. 9. Lower panel: Experimental resonant inelastic x-ray scattering (RIXS) spectrum (open green circles) measured by Ishii *et al.* [60] at the Ir  $L_3$  edge in  $\text{Sr}_2\text{IrO}_4$  compared with the theoretically calculated one in the GGA+SO+ $U$  approach ( $U_{\text{eff}} = 1.2$  eV). Upper panel: Theoretically calculated partial interband transitions at the Ir  $M_3$  edge in  $\text{Sr}_2\text{IrO}_4$ .

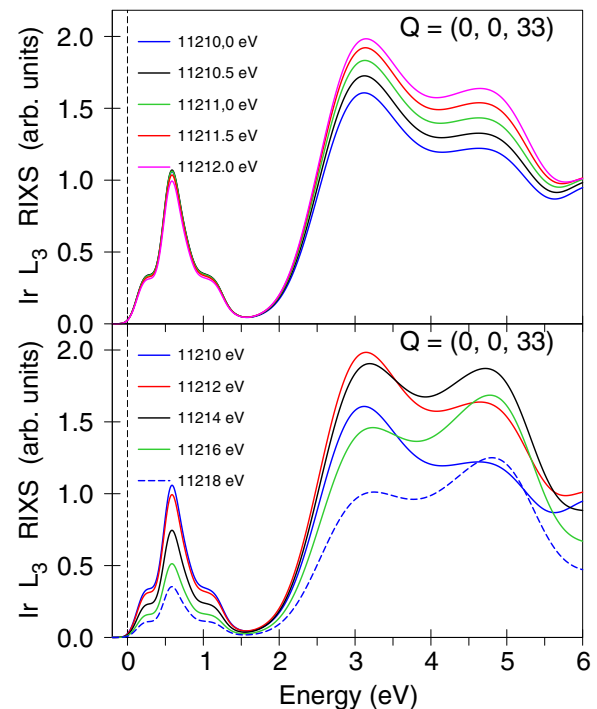


FIG. 10. The resonant inelastic x-ray scattering (RIXS) spectra as a function of incident photon energy  $E_i$  calculated at the Ir  $L_3$  edge in  $\text{Sr}_2\text{IrO}_4$  with the momentum transfer vector  $\mathbf{Q} = (0, 0, 33)$  in reciprocal lattice units.

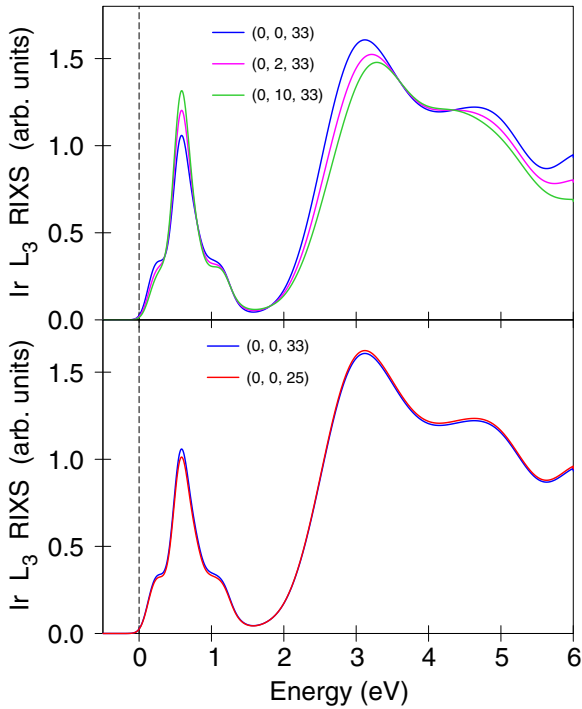


FIG. 11. The resonant inelastic x-ray scattering (RIXS) spectra at the Ir  $L_3$  edge in  $\text{Sr}_2\text{IrO}_4$  calculated as a function of  $Q_y$  (the upper panel) and  $Q_z$  (the lower panel) with the momentum transfer vector  $\mathbf{Q} = (0, Q_y, Q_z)$  in reciprocal lattice units for incident photon energy  $\hbar\omega_{\text{in}} = 11\,210$  eV.

3 eV and discovered that, with increasing  $E_i$ , the low-energy peak is decreased, but the high-energy peak is increased [for the same momentum transfer vector  $\mathbf{Q} = (0, 0, 33)$ ]. The lower panel of Fig. 10 shows the Ir  $L_3$  RIXS spectrum as a function of incident photon energy in the larger energy interval from 11 210 to 11 218 eV. With increasing  $E_i$ , the low-energy peak is steadily decreased, but the high-energy peak shows more complex behavior. First, the intensity of the peak is increased but then decreased with changing the relative intensity of the two peaks at 3 and 5 eV.

It is widely believed that  $d-d$  excitations show only small momentum transfer vector  $\mathbf{Q}$  dependence in  $5d$  transition metal compounds [45,109]. Particularly,  $\text{Sr}_2\text{IrO}_4$  has a layered-perovskite structure; therefore, the momentum dependence along the  $c$  axis is expected to be small, as in high- $T_c$  cuprates [110]. Indeed, as we see in the lower panel of Fig. 11, the RIXS spectra are almost identical for the transfer vectors  $\mathbf{Q} = (0, 0, 33)$  and  $(0, 0, 25)$ . Similar dependence was observed also in the measurements of Ishii *et al.* [60]. The upper panel of Fig. 11 shows the RIXS spectra at the Ir  $L_3$  edge in  $\text{Sr}_2\text{IrO}_4$  calculated as a function of  $Q_y$  with the momentum transfer vector  $\mathbf{Q} = (0, Q_y, 33)$  for incident photon energy  $\hbar\omega_{\text{in}} = 11\,210$  eV. We found that, with increasing  $Q_y$ , the first low-energy peak is increased, and the high-energy fine structure is decreased. Analyzing Fig. 11, we can conclude that the momentum dependence of the excitations in  $\text{Sr}_2\text{IrO}_4$  is rather small, as it was earlier observed in other iridates such as  $\text{Sr}_3\text{CuIrO}_6$  [45] or  $\text{In}_2\text{Ir}_2\text{O}_7$  [109].

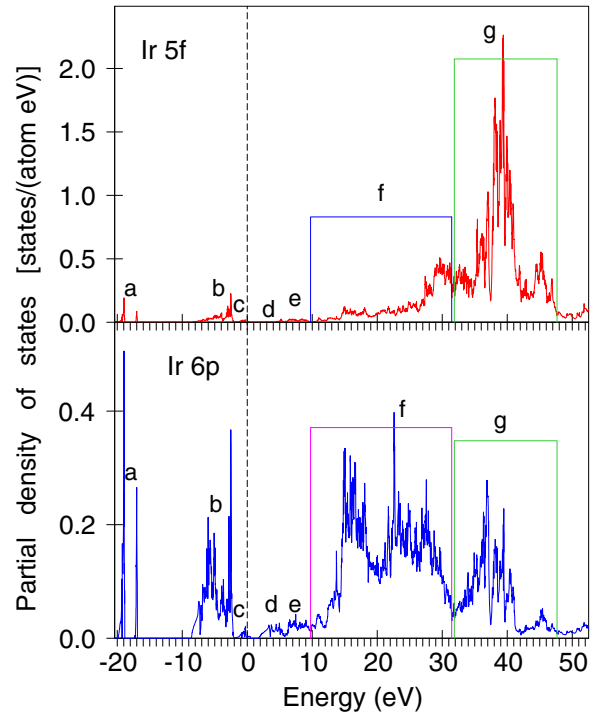


FIG. 12. The Ir  $6p$  (the lower panel) and  $5f$  (the upper panel) partial densities of states (DOSs) [in states/(atom eV)] in  $\text{Sr}_2\text{IrO}_4$  calculated in GGA+SO+ $U$  ( $U_{\text{eff}} = 1.2$  eV).

### B. $K$ and $M_5$ edges

Let us consider now the RIXS spectra at the Ir  $K$  and  $M_5$  edges. We present in Fig. 12 the Ir  $6p$  (the lower panel) and  $5f$  (the upper panel) partial DOSs in a wide energy interval from  $-20$  to  $52$  eV. We distinguish several groups of the bands. The group  $a$  is derived from the hybridization of Ir  $6p$  and  $5f$  states with oxygen  $2s$  states. The group  $b$  is due to the hybridization with oxygen  $2p$  states. The groups  $c$  and  $d$  are from the hybridization with the Ir  $t_{2g}$  LEB and UEB, respectively. The group  $e$  comes from the hybridization with Ir  $e_g$  states. The group  $f$  comes from the hybridization with Sr  $4f$  states. The structure  $g$  is the Ir  $5f$  bands themselves (the upper panel of Fig. 12) and the effect of the hybridization between Ir  $6p$  and  $5f$  states (the lower panel Fig. 12).

Figure 13 presents the theoretically calculated Ir  $K$  (the lower panel) and Ir  $M_5$  (the upper panel) RIXS spectra of  $\text{Sr}_2\text{IrO}_4$ . The spectra significantly differ from each other and from the RIXS spectra at the Ir  $L_3$  and  $M_3$  edges. The partial contributions from different interband transitions are also presented in Fig. 13. Due to significantly smaller spatial localization of the Ir  $5f$  orbitals in comparison with the  $6p$  one, the peaks  $a$ ,  $b$ ,  $c$ ,  $d$ , and  $e$ , which originate from the hybridization with oxygen  $2s$  and  $2p$  and Ir  $t_{2g}$  and  $e_g$  states, respectively, have much smaller intensity in the Ir  $5f$  partial DOSs in comparison with the Ir  $6p$  one (Fig. 12). However, transitions  $a + b + c \rightarrow d + e$  (the peak  $\alpha$ ) have similar intensity for both  $K$  and  $M_5$  spectra due to corresponding matrix elements. These peaks are much weaker, however, than the corresponding  $t_{2g} \rightarrow t_{2g}$ ,  $e_g$  transitions in the Ir  $L_3$  RIXS spectrum (Fig. 9). The major intensity in the Ir  $M_5$  RIXS spectrum comes from transitions between the  $b$ -type bands and the

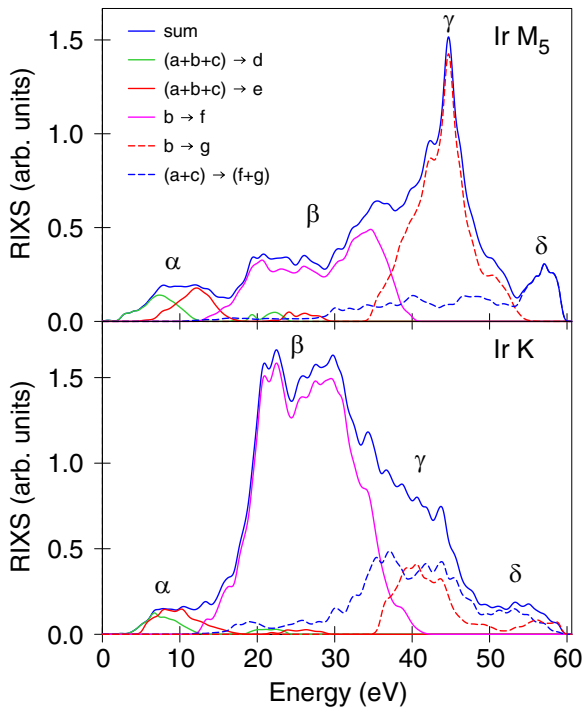


FIG. 13. The theoretically calculated resonant inelastic x-ray scattering (RIXS) spectrum of  $\text{Sr}_2\text{IrO}_4$  at the Ir  $K$  (the lower panel) and  $M_5$  (the upper panel) edges.

Ir  $5f$  bands ( $b \rightarrow g$ ). The small high-energy peak  $\delta$  is due to transitions  $a + c \rightarrow f + g$ . The largest contribution to the Ir  $K$  RIXS spectrum is made by interband transitions  $b \rightarrow f$  (the double peak  $\beta$ ). Such transitions are much weaker in the Ir  $M_5$  RIXS spectrum.

Experimental measurements of the RIXS spectra at the Ir  $K$  and  $M_5$  edges are highly desirable.

## V. O XAS AND RIXS SPECTRA

The RIXS spectra at the O  $K$  edge in  $\text{Sr}_2\text{IrO}_4$  were measured by Liu *et al.* [54], Lu *et al.* [57], Paris *et al.* [59], and Kim *et al.* [58]. The last three investigations concentrate on the analysis of low-energy excitations  $< 1.2$  eV. Liu *et al.* [54] presented the RIXS spectrum up to 12 eV using circular and  $\pi$  polarizations of the incident beam. The O  $K$  RIXS spectrum consists of a peak centered at zero energy loss, which comprises the elastic line and other low-energy features such as phonons, magnons, etc., and three major inelastic excitations at 0.7, 3.5, and  $\sim 6.2$  eV. We found that the first low-energy feature is due to the interband transitions between occupied and empty  $\text{O}_{t_{2g}}$  states, which appear as a result of the strong hybridization between oxygen  $2p$  states with Ir  $t_{2g}$  LEB and UEB in close vicinity to the Fermi level (see Fig. 6); therefore, the oxygen  $K$  RIXS spectroscopy can be used for the estimation of the energy band gap and positions of Ir  $5d$  Hubbard bands. The next two peaks at  $\sim 3.5$  and 6.2 eV reflect the interband transitions from the occupied O  $2p$  states and the empty oxygen states which originate from the hybridization with Ir  $t_{2g}$  and  $e_g$  states, respectively. We found that the theory reproduces well the shape and energy position of the low-energy

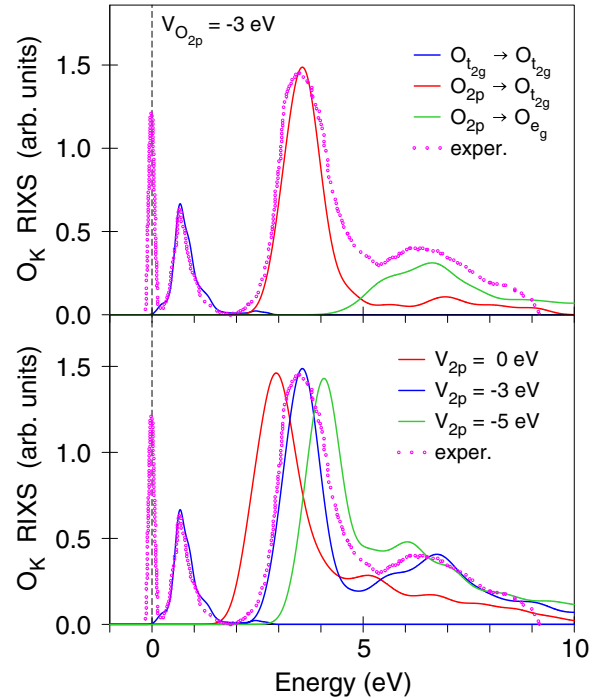


FIG. 14. (The upper panel) The experimental resonant inelastic x-ray scattering (RIXS) spectrum (open magenta circles) measured by Liu *et al.* [54] at the O  $K$  edge in  $\text{Sr}_2\text{IrO}_4$  compared with the theoretically calculated ones in the GGA+SO+ $U$ +SIC approach ( $U_{\text{eff}} = 1.2$  eV,  $V_{\text{O}2p} = -3$  eV). (The lower panel) The experimental RIXS spectrum (open magenta circles) measured by Liu *et al.* [54] at the O  $K$  edge in  $\text{Sr}_2\text{IrO}_4$  compared with the theoretically calculated ones in the GGA+SO+ $U$ +SIC approach ( $U_{\text{eff}} = 1.2$  eV) for different parameters  $V_l$ .

feature, but the second and third peaks are shifted toward smaller energy in comparison with the experimental measurements. It means that the DFT calculations cannot produce the correct energy position of the oxygen  $2p$  bands. These bands are almost fully occupied in  $\text{Sr}_2\text{IrO}_4$ ; therefore, they cannot be described by the GGA+ $U$  method. To reproduce the correct energy position of the oxygen  $2p$  band in  $\text{Sr}_2\text{IrO}_4$  we used a self-interaction-correction (SIC)-like procedure as proposed by Kaneko *et al.* [111], where the valence bands are shifted downward by adding a SIC-like orbital-dependent potential  $V_l$  into the Hamiltonian. We used  $V_l$  as an adjusted parameter to produce the correct energy position of the oxygen  $2p$  bands. We found that the best agreement with the experiment can be achieved for  $V_{\text{O}2p} = -3.0$  eV (see the lower panel of Fig. 14).

Figure 15 presents the valence band photoemission spectrum of  $\text{Sr}_2\text{IrO}_4$  [112] compared with the total DOS calculated in the GGA+SO+ $U$ +SIC approach ( $U_{\text{eff}} = 1.2$  eV). Two dominant peaks at around  $-1$  and  $-3.2$  eV are observed, which might be attributed to the photoemission from Ir  $t_{2g}$  and oxygen  $2p$  states, respectively [112]. Like in the case of O  $K$  RIXS spectrum, the GGA+SO+ $U$  approach cannot reproduce the correct energy position of the peak at  $-3.2$  eV. However, the SIC-like approach with  $V_{\text{O}2p} = -3$  eV improves the situation.

Figure 16 presents the RIXS spectra as a function of incident photon energy  $E_i$  calculated at the O  $K$  edge in

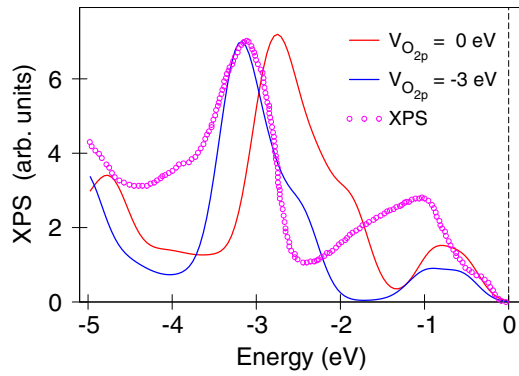


FIG. 15. The valence band photoemission spectrum of  $\text{Sr}_2\text{IrO}_4$  [112] compared with total density of states (DOS) calculated in the GGA+SO+ $U$ +SIC approach ( $U_{\text{eff}} = 1.2$  eV) for different parameters  $V_l$ .

$\text{Sr}_2\text{IrO}_4$  with circular polarization. We found much stronger dependence on the incident photon energy in the case of the O  $K$  RIXS spectrum in comparison with the corresponding dependence at the Ir  $L_3$  edge (compare Figs. 10 and 16). With increasing the incident photon energy, both peaks at 0.7 and 3.5 eV are increased; the latter one is increased dramatically. This occurs in a small energy interval for  $E_i$  of 0.6 eV from 529.0 to 529.6 eV.

Figure 17 shows the RIXS spectra at the O  $K$  edge in  $\text{Sr}_2\text{IrO}_4$  calculated as a function of  $Q_y$  (the upper panel) and  $Q_z$  (the lower panel) with the momentum transfer vector  $\mathbf{Q} = (0, Q_y, Q_z)$ . With decreasing parameters  $Q_x$  and  $Q_z$ , the intensity of the major peak at 3.5 eV is decreased, but the low-energy peak at 0.7 eV is increased. There is also a strong change in the shape of the low-energy peak at 0.7 eV and the third peak at  $\sim 6.2$  eV with the change of the parameter  $Q_z$ .

Figure 18 presents the experimental O  $K$  polarization-dependent XAS (open magenta circles) [4] compared with the theoretically calculated ones in the GGA+SO+ $U$ +SIC approach ( $U_{\text{eff}} = 1.2$  eV,  $V_{O_{2p}} = -3$  eV). Due to the quasi-2D structure of  $\text{Sr}_2\text{IrO}_4$ , there is strong anisotropy in the XAS. There are two small peaks  $a$  and  $b$  at 529.1 and 529.9 eV and a larger peak  $c$  at  $\sim 531.8$  eV for the  $\mathbf{E} \perp c$  polarization and

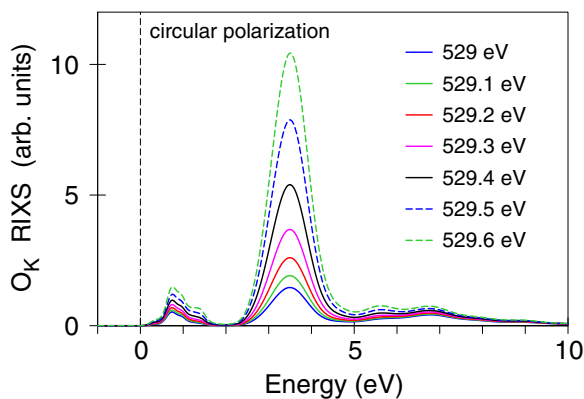


FIG. 16. The resonant inelastic x-ray scattering (RIXS) spectra as a function of incident photon energy calculated at the O  $K$  edge in  $\text{Sr}_2\text{IrO}_4$  with circular polarization.

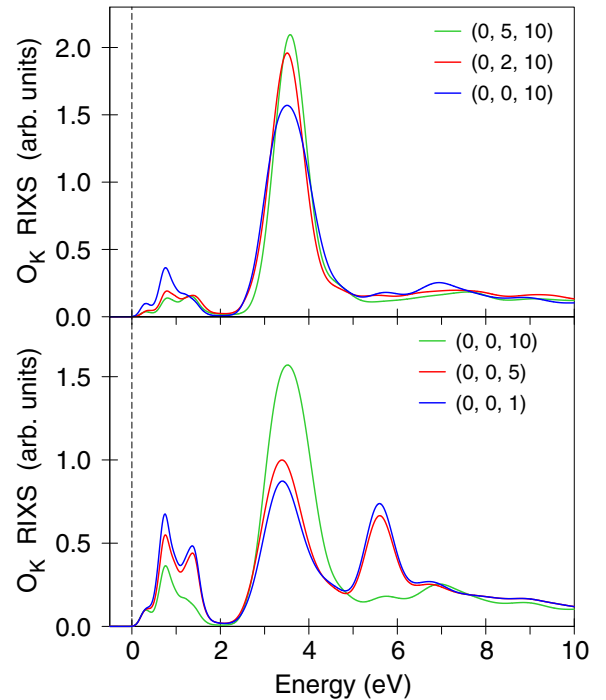


FIG. 17. The resonant inelastic x-ray scattering (RIXS) spectra at the O  $K$  edge in  $\text{Sr}_2\text{IrO}_4$  calculated as a function of  $Q_y$  (the upper panel) and  $Q_z$  (the lower panel) with the momentum transfer vector  $\mathbf{Q} = (0, Q_y, Q_z)$  in reciprocal lattice units for incident photon energy  $\hbar\omega_{\text{in}} = 529$  eV.

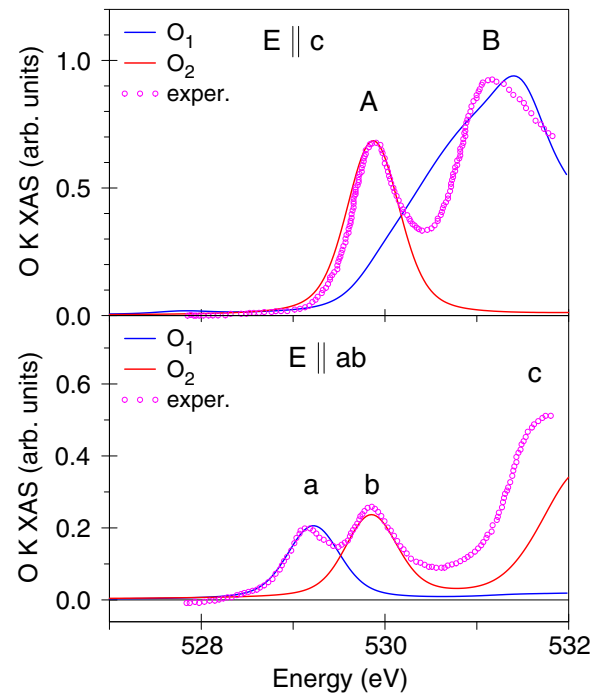


FIG. 18. The experimental O  $K$  polarization-dependent x-ray absorption spectroscopy (XAS) spectra (open magenta circles) [4] in  $\text{Sr}_2\text{IrO}_4$  compared with the theoretically calculated ones in the GGA+SO+ $U$ +SIC approach ( $U_{\text{eff}} = 1.2$  eV,  $V_{O_{2p}} = -3$  eV).

only two peaks *A* and *B* for  $\mathbf{E} \parallel c$  at 529.9 and 531.3 eV. We found that the low-energy peak *a* for  $\mathbf{E} \perp c$  and the large peak *B* for  $\mathbf{E} \parallel c$  are derived from the apical oxygens  $O_1$ . The peaks *b* and *A* are due to the  $1s \rightarrow 2p$  x-ray absorption by the in-plane  $O_2$  oxygens. The theory reproduces the experimentally measured XAS spectra relatively well.

## VI. CONCLUSIONS

To summarize, we have investigated the electronic and magnetic structures of  $Sr_2IrO_4$  in the frame of the fully relativistic spin-polarized Dirac approach. We have also presented comprehensive theoretical calculations of the XAS, XMCD, and RIXS spectra at the Ir  $K$ ,  $L_3$ ,  $M_3$ , and  $M_5$  and oxygen  $K$  edges.

The delicate interplay between electron correlations, SOC, intersite hoppings, and a crystal field splitting leads to a strongly competing ground state for  $Sr_2IrO_4$ . Although each Ir site accommodates five electrons,  $Sr_2IrO_4$  exhibits insulating behavior at all temperatures with an optical gap of  $\Delta \leq 0.4$  eV at room temperature. Below 240 K, canted AFM order sets in, with a small FM saturation moment. Our band structure calculations show that the canted NC AFM configuration with the spins in the *ab* plane possesses the lowest total energy in comparison with the nonmagnetic, FM, or AFM configuration along the *c* direction. Small net magnetization in  $Sr_2IrO_4$  can be explained by the canted AFM solution.

A remarkably large branching ratio  $BR = I_{L_3}/I_{L_2} = 3.56$  indicates a strong SO effect in  $Sr_2IrO_4$ . Strong SOC splits the  $t_{2g}$  manifold into a lower  $J_{\text{eff}} = \frac{3}{2}$  quartet and an upper  $J_{\text{eff}} = \frac{1}{2}$  doublet. The functions of the  $J_{\text{eff}} = \frac{3}{2}$  quartet are dominated by  $d_{3/2}$  states with some weight of  $d_{5/2}$  ones, and the  $J_{\text{eff}} = \frac{1}{2}$  functions are almost completely given by linear combinations of  $d_{5/2}$  states.

The energy gap in  $Sr_2IrO_4$  opens up only with considering Hubbard electron-electron correlations, but on the other hand, the value of  $U_{\text{eff}}^c$  strongly depends on the magnetic ordering; therefore,  $Sr_2IrO_4$  has mixed Slater and Mott character representing the uniqueness of  $Sr_2IrO_4$ .

The theoretically calculated Ir  $L_3$  RIXS spectrum is in good agreement with the experiment. We found that the low-energy peak corresponds to intra- $t_{2g}$  excitations. This fine structure

has a two-peak structure. The low-energy peak at 0.2 eV is due to interband transitions between occupied and empty Ir  $J_{\text{eff}} = \frac{1}{2}$  states. These transitions also contribute to the second high-energy peak at  $\sim 0.6$  eV together with  $J_{3/2} \rightarrow J_{1/2}$  transitions. The intensive peak at  $\sim 3.4$  eV is due to  $t_{2g} \rightarrow e_g$  transitions. The next fine structure from 4.5 to 12 eV is due to  $5d_O \rightarrow (t_{2g} + e_g)$  transitions. Due to the strong dependence of the RIXS spectrum at the Ir  $L_3$  edge on the momentum transfer vector  $\mathbf{Q}$  and polarization, some measurements show additional peaks  $< 0.6$  eV at specific geometry conditions and very high instrumental resolution. These peaks can be attributed to exciton and magnon excitations. The theoretical investigation of such excitations demands special consideration beyond the one-particle approximation.

The RIXS spectrum of  $Sr_2IrO_4$  at the O  $K$  edge consists of three major inelastic excitations at 0.7, 3.5, and  $\sim 6.2$  eV. We found that the first low-energy feature is due to interband transitions between occupied and empty  $O_{t_{2g}}$  states, which appear as a result of the strong hybridization between oxygen  $2p$  states with Ir  $t_{2g}$  LEB and UEB in close vicinity to the Fermi level. The next two peaks at  $\sim 3.5$  and 6.2 eV reflect the interband transitions from the occupied O  $2p$  states to the empty oxygen states which originate from the hybridization with Ir  $t_{2g}$  and  $e_g$  states, respectively. We found that the theory reproduces well the shape and energy position of the low-energy feature, but to obtain the correct positions of the second and third peaks, a SIC-like orbital-dependent potential  $V_l$  must be included into the Hamiltonian to correct the position of the oxygen  $2p$  band.

The RIXS spectra at the Ir  $K$  and  $M_5$  edges occupy a very wide energy interval up to 60 eV which is almost six times larger than, for example, the occupation of the Ir  $L_3$  and  $M_3$  or oxygen  $K$  spectra. The major contributions to the Ir  $M_5$  RIXS spectrum comes from interband transitions into empty Ir  $5f$  bands. The Ir  $K$  spectrum reflects the energy distribution of different states (oxygen  $2s$  and  $2p$ , Ir  $5d$  and  $5f$ , and Sr  $4d$  and  $4f$ ) due to extended character of Ir  $6p$  orbitals. The experimental measurements of the RIXS spectra at the Ir  $K$  and  $M_5$  edges can be very prospective in the near future.

## ACKNOWLEDGMENT

We are thankful to Dr. Alexander Yaresko from the Max Planck Institute FKF in Stuttgart for helpful discussions.

- 
- [1] G. Jackeli and G. Khaliullin, *Phys. Rev. Lett.* **102**, 017205 (2009).
  - [2] G. Chen, R. Pereira, and L. Balents, *Phys. Rev. B* **82**, 174440 (2010).
  - [3] W. Witczak-Krempa, G. Chen, Y. B. Kim, and L. Balents, *Annu. Rev. Condens. Matter Phys.* **5**, 57 (2014).
  - [4] B. J. Kim, H. Jin, S. J. Moon, J.-Y. Kim, B.-G. Park, C. S. Leem, J. Yu, T. W. Noh, C. Kim, S.-J. Oh *et al.*, *Phys. Rev. Lett.* **101**, 076402 (2008).
  - [5] C. Martins, M. Aichhorn, L. Vaugier, and S. Biermann, *Phys. Rev. Lett.* **107**, 266404 (2011).
  - [6] V. N. Antonov, S. Uba, and L. Uba, *Phys. Rev. B* **98**, 245113 (2018).
  - [7] X.-L. Qi and S.-C. Zhang, *Phys. Today* **63**(1), 33 (2010).
  - [8] Y. Ando, *J. Phys. Soc. Jpn.* **82**, 102001 (2013).
  - [9] T. O. Wehling, A. Black-Schafferc, and A. Balatsky, *Adv. Phys.* **63**, 1 (2014).
  - [10] A. Bansil, H. Lin, and T. Das, *Rev. Mod. Phys.* **88**, 021004 (2016).
  - [11] B. J. Kim, H. Ohsumi, T. Komesu, S. Sakai, T. Morita, H. Takagi, and T. Arima, *Science* **323**, 1329 (2009).
  - [12] H. Watanabe, T. Shirakawa, and S. Yunoki, *Phys. Rev. Lett.* **105**, 216410 (2010).
  - [13] W. Witczak-Krempa and Y. B. Kim, *Phys. Rev. B* **85**, 045124 (2012).

- [14] A. Go, W. Witczak-Krempa, G. S. Jeon, K. Park, and Y. B. Kim, *Phys. Rev. Lett.* **109**, 066401 (2012).
- [15] A. B. Sushkov, J. B. Hofmann, G. S. Jenkins, J. Ishikawa, S. Nakatsuji, S. Das Sarma, and H. D. Drew, *Phys. Rev. B* **92**, 241108(R) (2015).
- [16] I. Kimchi, J. G. Analytis, and A. Vishwanath, *Phys. Rev. B* **90**, 205126 (2014).
- [17] Y. J. Yan, M. Q. Ren, H. C. Xu, B. P. Xie, R. Tao, H. Y. Choi, N. Lee, Y. J. Choi, T. Zhang, and D. L. Feng, *Phys. Rev. X* **5**, 041018 (2015).
- [18] I. Battisti, K. M. Bastiaans, V. Fedoseev, A. de la Torre, N. Iliopoulos, A. Tamai, E. C. Hunter, R. S. Perry, J. Zaanen, F. Baumberger *et al.*, *Nat. Phys.* **13**, 21 (2017).
- [19] A. Damascelli, Z. Hussain, and Z.-X. Shen, *Rev. Mod. Phys.* **75**, 473 (2003).
- [20] Y. K. Kim, O. Krupin, J. D. Denlinger, A. Bostwick, E. Rotenberg, Q. Zhao, J. F. Mitchell, J. W. Allen, and B. J. Kim, *Science* **345**, 187 (2014).
- [21] Y. K. Kim, N. H. Sung, J. D. Denlinger, and B. J. Kim, *Nat. Phys.* **12**, 37 (2016).
- [22] K. Terashima, M. Sunagawa, H. Fujiwara, T. Fukura, M. Fujii, K. Okada, K. Horigane, K. Kobayashi, R. Horie, J. Akimitsu *et al.*, *Phys. Rev. B* **96**, 041106(R) (2017).
- [23] Y. Hu, X. Chen, S. T. Peng, C. Lane, M. Matzelle, Z. L. Sun, M. Hashimoto, D. H. Lu, E. F. Schwier, M. Arita *et al.*, *Phys. Rev. Lett.* **123**, 216402 (2019).
- [24] J. Kim, D. Casa, M. H. Upton, T. Gog, Y.-J. Kim, J. F. Mitchell, M. van Veenendaal, M. Daghofer, J. van den Brink, G. Khaliullin *et al.*, *Phys. Rev. Lett.* **108**, 177003 (2012).
- [25] J. P. Clancy, H. Gretarsson, M. H. Upton, J. Kim, G. Cao, and Y.-J. Kim, *Phys. Rev. B* **100**, 104414 (2019).
- [26] J. Bertinshaw, Y. Kim, G. Khaliullin, and B. Kim, *Annu. Rev. Condens. Matter Phys.* **10**, 315 (2019).
- [27] S. J. Moon, H. Jin, W. S. Choi, J. S. Lee, S. S. A. Seo, J. Yu, G. Cao, T. W. Noh, and Y. S. Lee, *Phys. Rev. B* **80**, 195110 (2009).
- [28] H. Jin, H. Jeong, T. Ozaki, and J. Yu, *Phys. Rev. B* **80**, 075112 (2009).
- [29] R. Arita, J. Kuneš, A. V. Kozhevnikov, A. G. Eguiluz, and M. Imada, *Phys. Rev. Lett.* **108**, 086403 (2012).
- [30] Q. Wang, Y. Cao, J. A. Waugh, S. R. Park, T. F. Qi, O. B. Korneta, G. Cao, and D. S. Dessau, *Phys. Rev. B* **87**, 245109 (2013).
- [31] H. Zhang, K. Haule, and D. Vanderbilt, *Phys. Rev. Lett.* **111**, 246402 (2013).
- [32] J. L. Lado and V. Pardo, *Phys. Rev. B* **92**, 155151 (2015).
- [33] Y. Liu, L. Yu, X. Jia, J. Zhao, H. Weng, Y. Peng, C. Chen, Z. Xie, D. Mou, J. He *et al.*, *Sci. Rep.* **5**, 13036 (2015).
- [34] V. M. Katukuri, R. Yadav, L. Hozoi, S. Nishimoto, and J. van den Brink, *Sci. Rep.* **6**, 29585 (2016).
- [35] J. Cheng, X. Sun, S. Liu, B. Li, H. Wang, P. Dong, Y. Wang, and W. Xu, *New J. Phys.* **18**, 093019 (2016).
- [36] S. Mohapatra, J. van den Brink, and A. Singh, *Phys. Rev. B* **95**, 094435 (2017).
- [37] C. Martins, M. Aichhorn, and S. Biermann, *J. Phys.: Condens. Matter* **29**, 263001 (2017).
- [38] B. Lenz, C. Martins, and S. Biermann, *J. Phys.: Condens. Matter* **31**, 293001 (2019).
- [39] C. Bhandari, Z. S. Popovic, and S. Satpathy, *New J. Phys.* **21**, 013036 (2019).
- [40] V. Singh and J. J. Pulikkotil, *J. Phys.: Condens. Matter* **31**, 425501 (2019).
- [41] P. Liu and C. Franchini, *Appl. Sci.* **11**, 2527 (2021).
- [42] C. H. Sohn, H. S. Kim, T. F. Qi, D. W. Jeong, H. J. Park, H. K. Yoo, H. H. Kim, J. Y. Kim, T. D. Kang, D. Y. Cho *et al.*, *Phys. Rev. B* **88**, 085125 (2013).
- [43] C.-C. Kao, W. A. L. Caliebe, J. B. Hastings, and J.-M. Gillet, *Phys. Rev. B* **54**, 16361 (1996).
- [44] L. J. P. Ament, M. van Veenendaal, T. P. Devereaux, J. P. Hill, and J. van den Brink, *Rev. Mod. Phys.* **83**, 705 (2011).
- [45] X. Liu, V. M. Katukuri, L. Hozoi, W.-G. Yin, M. P. M. Dean, M. H. Upton, J. Kim, D. Casa, A. Said, T. Gog *et al.*, *Phys. Rev. Lett.* **109**, 157401 (2012).
- [46] L. Hozoi, H. Gretarsson, J. P. Clancy, B.-G. Jeon, B. Lee, K. H. Kim, V. Yushankhai, P. Fulde, D. Casa, T. Gog *et al.*, *Phys. Rev. B* **89**, 115111 (2014).
- [47] J. P. Clancy, H. Gretarsson, E. K. H. Lee, D. Tian, J. Kim, M. H. Upton, D. Casa, T. Gog, Z. Islam, B.-G. Jeon *et al.*, *Phys. Rev. B* **94**, 024408 (2016).
- [48] A. Nag, S. Bhowal, A. Chakraborty, M. M. Sala, A. Efimenko, F. Bert, P. K. Biswas, A. D. Hillier, M. Itoh, S. D. Kaushik *et al.*, *Phys. Rev. B* **98**, 014431 (2018).
- [49] T. Takayama, A. Krajewska, A. S. Gibbs, A. N. Yaresko, H. Ishii, H. Yamaoka, K. Ishii, N. Hiraoka, N. P. Funnell, C. L. Bull *et al.*, *Phys. Rev. B* **99**, 125127 (2019).
- [50] A. A. Aczel, Q. Chen, J. P. Clancy, C. dela Cruz, D. Reig-i-Plessis, G. J. MacDougall, C. J. Pollock, M. H. Upton, T. J. Williams, N. LaManna *et al.*, *Phys. Rev. Mater.* **6**, 094409 (2022).
- [51] S. Calder, J. Vale, N. Bogdanov, X. Liu, C. Donnerer, M. Upton, D. Casa, A. Said, M. Lumsden, Z. Zhao *et al.*, *Nat. Commun.* **7**, 11651 (2016).
- [52] A. E. Taylor, S. Calder, R. Morrow, H. L. Feng, M. H. Upton, M. D. Lumsden, K. Yamaura, P. M. Woodward, and A. D. Christianson, *Phys. Rev. Lett.* **118**, 207202 (2017).
- [53] S. Calder, J. G. Vale, N. Bogdanov, C. Donnerer, D. Pincini, M. Moretti Sala, X. Liu, M. H. Upton, D. Casa, Y.G. Shi *et al.*, *Phys. Rev. B* **95**, 020413(R) (2017).
- [54] X. Liu, M. P. M. Dean, J. Liu, S. G. Chiuzbaian, N. Jaouen, A. Nicolaou, W. G. Yin, C. R. Serrao, R. Ramesh, H. Ding *et al.*, *J. Phys.: Condens. Matter* **27**, 202202 (2015).
- [55] C. Monney, M. Herzog, A. Pulkkinen, Y. Huang, J. Pellicciari, P. Olalde-Velasco, N. Katayama, M. Nohara, H. Takagi, T. Schmitt *et al.*, *Phys. Rev. B* **102**, 085148 (2020).
- [56] W. S. Lee, S. Johnston, B. Moritz, J. Lee, M. Yi, K. J. Zhou, T. Schmitt, L. Patthey, V. Strocov, K. Kudo *et al.*, *Phys. Rev. Lett.* **110**, 265502 (2013).
- [57] X. Lu, P. Olalde-Velasco, Y. Huang, V. Bisogni, J. Pellicciari, S. Fatale, M. Dantz, J. G. Vale, E. C. Hunter, J. Chang *et al.*, *Phys. Rev. B* **97**, 041102(R) (2018).
- [58] J.-K. Kim, C. Dietl, H.-W. J. Kim, S.-H. Ha, J. Kim, A. H. Said, J. Kim, and B. J. Kim, *J. Synchrotron Radiat.* **30**, 643 (2023).
- [59] E. Paris, Y. Tseng, E. M. Pärshcke, W. Zhang, M. H. Upton, A. Efimenko, K. Rolfs, D. E. McNally, L. Maurel, M. Naamneh *et al.*, *Proc. Natl. Acad. Sci. USA* **117**, 24764 (2020).
- [60] K. Ishii, I. Jarrige, M. Yoshida, K. Ikeuchi, J. Mizuki, K. Ohashi, T. Takayama, J. Matsuno, and H. Takagi, *Phys. Rev. B* **83**, 115121 (2011).

- [61] A. Lupascu, J. P. Clancy, H. Gretarsson, Z. Nie, J. Nichols, J. Terzic, G. Cao, S. S. A. Seo, Z. Islam, M. H. Upton *et al.*, *Phys. Rev. Lett.* **112**, 147201 (2014).
- [62] J. Bertinshaw, J. K. Kim, J. Porras, K. Ueda, N. H. Sung, A. Efimenko, A. Bombardi, J. Kim, B. Keimer, and B. J. Kim, *Phys. Rev. B* **101**, 094428 (2020).
- [63] J. P. Clancy, H. Gretarsson, A. Lupascu, J. A. Sears, Z. Nie, M. H. Upton, J. Kim, Z. Islam, M. Uchida, D. G. Schlom *et al.*, *Phys. Rev. B* **107**, 054423 (2023).
- [64] G. Y. Guo, H. Ebert, W. M. Temmerman, and P. J. Durham, *Phys. Rev. B* **50**, 3861 (1994).
- [65] V. Antonov, B. Harmon, and A. Yaresko, *Electronic Structure and Magneto-Optical Properties of Solids* (Kluwer, Dordrecht, 2004).
- [66] E. Arola, M. Horne, P. Strange, H. Winter, Z. Szotek, and W. M. Temmerman, *Phys. Rev. B* **70**, 235127 (2004).
- [67] V. V. Nemoshkalenko, A. E. Krasovskii, V. N. Antonov, V. N. Antonov, U. Fleck, H. Wonn, and P. Ziesche, *Phys. Status Solidi B* **120**, 283 (1983).
- [68] E. Arola, P. Strange, and B. L. Gyorffy, *Phys. Rev. B* **55**, 472 (1997).
- [69] V. N. Antonov, D. A. Kukusta, and L. V. Bekenov, *Phys. Rev. B* **105**, 155144 (2022).
- [70] T. Shimura, Y. Inaguma, T. Nakamura, M. Itoh, and Y. Morii, *Phys. Rev. B* **52**, 9143 (1995).
- [71] V. N. Antonov, O. Jepsen, A. N. Yaresko, and A. P. Shpak, *J. Appl. Phys.* **100**, 043711 (2006).
- [72] V. N. Antonov, B. N. Harmon, A. N. Yaresko, and A. P. Shpak, *Phys. Rev. B* **75**, 184422 (2007).
- [73] V. N. Antonov, A. N. Yaresko, and O. Jepsen, *Phys. Rev. B* **81**, 075209 (2010).
- [74] O. K. Andersen, *Phys. Rev. B* **12**, 3060 (1975).
- [75] J. P. Perdew, K. Burke, and M. Ernzerhof, *Phys. Rev. Lett.* **77**, 3865 (1996).
- [76] P. E. Blöchl, O. Jepsen, and O. K. Andersen, *Phys. Rev. B* **49**, 16223 (1994).
- [77] A. N. Yaresko, V. N. Antonov, and P. Fulde, *Phys. Rev. B* **67**, 155103 (2003).
- [78] P. H. Dederichs, S. Blügel, R. Zeller, and H. Akai, *Phys. Rev. Lett.* **53**, 2512 (1984).
- [79] W. E. Pickett, S. C. Erwin, and E. C. Ethridge, *Phys. Rev. B* **58**, 1201 (1998).
- [80] V. N. Antonov, D. A. Kukusta, and L. V. Bekenov, *Phys. Rev. B* **105**, 155145 (2022).
- [81] S. Boseggia, H. C. Walker, J. Vale, R. Springell, Z. Feng, R. S. Perry, M. M. Sala, H. M. Ronnow, S. P. Collins, and D. F. McMorrow, *J. Phys.: Condens. Matter* **25**, 422202 (2013).
- [82] F. Ye, S. Chi, B. C. Chakoumakos, J. A. Fernandez-Baca, T. Qi, and G. Cao, *Phys. Rev. B* **87**, 140406(R) (2013).
- [83] P. Liu, S. Khmelevskiy, B. Kim, M. Marsman, D. Li, X.-Q. Chen, D. D. Sarma, G. Kresse, and C. Franchini, *Phys. Rev. B* **92**, 054428 (2015).
- [84] S. Fujiyama, H. Ohsumi, T. Komesu, J. Matsuno, B. J. Kim, M. Takata, T. Arima, and H. Takagi, *Phys. Rev. Lett.* **108**, 247212 (2012).
- [85] N. S. Kini, A. M. Strydom, H. S. Jeevan, C. Geibel, and S. Ramakrishnan, *J. Phys.: Condens. Matter* **18**, 8205 (2006).
- [86] Q. Li, G. Cao, S. Okamoto, J. Yi, W. Lin, B. C. Sales, J. Yan, R. Arita, J. Kunes, A. V. Kozhevnikov *et al.*, *Sci. Rep.* **3**, 3073 (2013).
- [87] A. Yamasaki, S. Tachibana, H. Fujiwara, A. Higashiya, A. Irizawa, O. Kirilmaz, F. Pfaff, P. Scheiderer, J. Gabel, M. Sing *et al.*, *Phys. Rev. B* **89**, 121111(R) (2014).
- [88] S. Chikara, O. Korneta, W. P. Crummett, L. E. DeLong, P. Schlottmann, and G. Cao, *Phys. Rev. B* **80**, 140407(R) (2009).
- [89] J. Nichols, N. Bray-Ali, A. Ansary, G. Cao, and K.-W. Ng, *Phys. Rev. B* **89**, 085125 (2014).
- [90] J. Dai, E. Calleja, G. Cao, and K. McElroy, *Phys. Rev. B* **90**, 041102(R) (2014).
- [91] D. Hsieh, F. Mahmood, D. H. Torchinsky, G. Cao, and N. Gedik, *Phys. Rev. B* **86**, 035128 (2012).
- [92] J.-M. Carter and H.-Y. Kee, *Phys. Rev. B* **87**, 014433 (2013).
- [93] H. Watanabe, T. Shirakawa, and S. Yunoki, *Phys. Rev. B* **89**, 165115 (2014).
- [94] D. D. Koelling and B. N. Harmon, *J. Phys. C* **10**, 3107 (1977).
- [95] D. Pröpper, A. N. Yaresko, M. Höppner, Y. Matiks, Y.-L. Mathis, T. Takayama, A. Matsumoto, H. Takagi, B. Keimer, and A. V. Boris, *Phys. Rev. B* **94**, 035158 (2016).
- [96] B. H. Kim, G. Khaliullin, and B. I. Min, *Phys. Rev. Lett.* **109**, 167205 (2012).
- [97] J. P. Perdew and Y. Wang, *Phys. Rev. B* **45**, 13244 (1992).
- [98] D. Haskel, G. Fabbri, M. Zhernenkov, P. P. Kong, C. Q. Jin, G. Cao, and M. van Veenendaal, *Phys. Rev. Lett.* **109**, 027204 (2012).
- [99] G. van der Laan and B. T. Thole, *Phys. Rev. Lett.* **60**, 1977 (1988).
- [100] J. Kim, M. Daghofer, A. H. Said, T. Gog, J. van den Brink, G. Khaliullin, and B. J. Kim, *Nat. Commun.* **5**, 4453 (2014).
- [101] J. Kim, A. H. Said, D. Casa, M. H. Upton, T. Gog, M. Daghofer, G. Jackeli, J. van den Brink, G. Khaliullin, and B. J. Kim, *Phys. Rev. Lett.* **109**, 157402 (2012).
- [102] M. MorettiSala, V. Schnells, S. Boseggia, L. Simonelli, A. Al-Zein, J. G. Vale, L. Paolasini, E. C. Hunter, R. S. Perry, D. Prabhakaran *et al.*, *Phys. Rev. B* **92**, 024405 (2015).
- [103] H. Gretarsson, N. H. Sung, J. Porras, J. Bertinshaw, C. Dietl, J. A. N. Bruin, A. F. Bangura, Y. K. Kim, R. Dinnebier, J. Kim *et al.*, *Phys. Rev. Lett.* **117**, 107001 (2016).
- [104] X. Lu, D. E. McNally, M. Moretti Sala, J. Terzic, M. H. Upton, D. Casa, G. Ingold, G. Cao, and T. Schmitt, *Phys. Rev. Lett.* **118**, 027202 (2017).
- [105] J. I. Igarashi and T. Nagao, *Phys. Rev. B* **90**, 064402 (2014).
- [106] S. Mohapatra and A. Singh, *arXiv:1903.03360*.
- [107] S. Mohapatra and A. Singh, *J. Magn. Magn. Mater.* **512**, 166997 (2020).
- [108] M. Ge, T. F. Qi, O. B. Korneta, D. E. D. Long, P. Schlottmann, W. P. Crummett, and G. Cao, *Phys. Rev. B* **84**, 100402(R) (2011).
- [109] A. Krajewska, T. Takayama, R. Dinnebier, A. Yaresko, K. Ishii, M. Isobe, and H. Takagi, *Phys. Rev. B* **101**, 121101(R) (2020).
- [110] K. Ishii, K. Tsutsui, Y. Endoh, T. Tohyama, S. Maekawa, M. Hoesch, K. Kuzushita, M. Tsubota, T. Inami, J. Mizuki *et al.*, *Phys. Rev. Lett.* **94**, 207003 (2005).
- [111] T. Kaneko, T. Toriyama, T. Konishi, and Y. Ohta, *Phys. Rev. B* **87**, 035121 (2013).
- [112] P. D. C. King, T. Takayama, A. Tamai, E. Rozbicki, S. M. Walker, M. Shi, L. Patthey, R. G. Moore, D. Lu, K. M. Shen *et al.*, *Phys. Rev. B* **87**, 241106(R) (2013).